Available online at www.sciencedirect.com

ScienceDirect

Geochimica et Cosmochimica Acta 331 (2022) 165–191

Geochimica et Cosmochimica Acta

www.elsevier.com/locate/gca

Microbial Fe cycling in a simulated Precambrian ocean environment: Implications for secondary mineral (trans)formation and deposition during BIF genesis

Manuel Schad [a,b,*], James M. Byrne [a,1], Laurel K. ThomasArrigo [c], Ruben Kretzschmar [c], Kurt O. Konhauser [b], Andreas Kappler [a,d]

[a] *Geomicrobiology, Center for Applied Geosciences, University of Tuebingen, Tuebingen, Germany*
[b] *Department of Earth and Atmospheric Sciences, University of Alberta, Edmonton, Canada*
[c] *Soil Chemistry, Department of Environmental Systems Science, ETH Zuerich, Zuerich, Switzerland*
[d] *Cluster of Excellence: EXC 2124: Controlling Microbes to Fight Infection, Tuebingen, Germany*

Received 8 July 2021; accepted in revised form 18 May 2022; Available online 21 May 2022

Abstract

Banded Iron Formations (BIFs) are ancient marine chemical sediments that contain various Fe-bearing minerals such as hematite (Fe_2O_3), magnetite (Fe_3O_4), siderite ($FeCO_3$) and a variety of Fe^{II}-/Fe^{III}-silicates. The prevailing opinion is that primary Fe(III) (oxyhydr)oxides, such as ferrihydrite (simplified formula of $Fe(OH)_3$), were precipitated from the ocean's photic zone by marine plankton, and a fraction of these minerals was subsequently transformed into secondary magnetite and siderite by dissimilatory Fe(III)-reducing bacteria (DIRB). However, aside from broad estimates, it is currently unknown what fraction of the primary Fe(III) minerals was sedimented to the seafloor where it was eventually lithified, and what fraction was reduced by DIRB in the water column, thus forming a microbial Fe cycle in the water column. To test this, we conducted Fe cycling experiments with marine phototrophic Fe(II)-oxidizing bacteria and DIRB under conditions mimicking the Precambrian ocean water column with elevated Fe(II) and Si concentrations. We followed secondary mineral formation over three consecutive redox cycles (oxidation followed by reduction) over a time interval of up to 58 days to determine which mineral phases would ultimately have settled as BIF forming sediments. We used wet geochemical methods to follow Fe speciation, measured dissolved silica and volatile fatty acid (VFA) concentrations, determined cell-mineral associations using fluorescence and electron microscopy, and characterized the mineralogy of the precipitates using ^{57}Fe-Moessbauer spectroscopy and X-ray diffraction (XRD). Our results showed that both the absence of silica and an increasing number of Fe cycles favored the formation of more crystalline minerals, such as goethite (α-FeOOH). However, in the presence of high concentrations of monomeric silica, as suggested for ancient oceans (2.2 mM), only short-range ordered (SRO) Fe(III) minerals such as ferrihydrite were observed. These did not transform into the more thermodynamically stable goethite during repeated Fe cycling. Interestingly, no magnetite formed in any of the setups. Instead, increasing Si concentrations favored the formation of increasing quantities of Fe(II) minerals. Microscopy revealed a tight association between microbial biomass and minerals formed. Dissolved silica analysis showed the removal of Si from solution congruent with Fe(II) oxidation and a release of Si during Fe(III) reduction. Together, these results suggest an important role of co-precipitated biomass as well as silica for secondary mineral formation by either constraining crystal growth and/or inhibiting Fe(II)-induced mineral transformation. Overall, our results imply that microbial Fe cycling during settling of primary ferrihydrite through the photic zone in a Precambrian ocean would have resulted in the partial transformation of ferrihydrite into secondary Fe(II) mineral phases in

* Corresponding author at: 3-11 Earth Sciences Building, University of Alberta, Edmonton, AB T6G 2E3, Canada.
E-mail address: schad.science@gmail.com (M. Schad).
[1] Present address: School of Earth Sciences, University of Bristol, Bristol, United Kingdom.

https://doi.org/10.1016/j.gca.2022.05.016

the water column. This would have resulted in the accumulation of mixtures of a ferrihydrite-silica composite and Fe(II) minerals in the initial BIF forming sediments.

Keywords: Photoferrotrophy; Ferrous iron oxidation; Ferric iron reduction; Fe(III) minerals; Secondary mineral formation; Fe cycling; Banded Iron Formations

1. INTRODUCTION

The geochemistry of the Archean to early Paleoproterozoic ocean was fundamentally different from the modern ocean. Prior to the Great Oxidation Event (GOE) between 2.46 and 2.22 billion years ago (Gumsley et al, 2017; Poulton et al., 2021), when the Earth's atmosphere accumulated significant levels of oxygen for the first time (Lyons et al., 2014), the bulk ocean was essentially anoxic with O_2 concentrations below 1 μM (Olson et al., 2013; Hardisty et al., 2014). However, the water column above some continental shelf areas may already have been fully oxygenated 100 million years earlier (Kendall et al., 2010; Ostrander et al., 2019). Low O_2 in the bulk oceans, in combination with low sulfate/sulfide concentrations (Crowe et al., 2014) and an increased hydrothermal Fe flux (Kump and Seyfried, 2005), enabled the buildup of high concentrations of hydrothermally derived dissolved Fe(II) (Fe^{2+}) of between 0.03 and 0.5 mM (Holland, 1973; Morris, 1993), and potentially up to several mM (Derry, 2015; Jiang and Tosca, 2019). Similarly, the early ocean would have been enriched in dissolved Si, ranging from 0.67 mM (saturation with respect cristobalite) to 2.2 mM (saturation with respect to amorphous silica; Siever, 1992; Maliva et al., 2005), although a recent study suggested lower concentrations (0.5–1.6 mM; Zheng et al., 2016).

These conditions are reflected in the general composition of banded iron formations (BIFs); marine chemical sedimentary deposits which were mainly deposited during the Neoarchean and early Paleoproterozoic (Bekker et al., 2010, 2014; Konhauser et al., 2017). They predominantly consist of Fe (15–40 wt.%) and Si (40–60 wt.%; Trendall, 2002) deposited in alternating layers resulting in the characteristic banding (Trendall and Blockley, 1970). BIFs contain little organic carbon (<0.5 wt.%; Gole and Klein, 1981) and minimal detrital input (<1 wt.% Al_2O_3, <20 ppm Ti, Zr, Th, Hf, Sc; Konhauser et al., 2017). Their chemical composition, lateral continuity, high degree of preservation and general association with carbonates and shales suggest that BIFs were deposited in shelf environments on the margins of stable cratons. However, the absence of wave-generated structures indicates deposition in waters below wave base, deeper than 10 s–200 m (Isley, 1995; Trendall, 2002). Mineralogically, the least metamorphosed BIFs consist of hematite, magnetite, carbonates (ankerite, siderite) and chert with varying contributions of $Fe^{II}Fe^{III}$-silicates (e.g., greenalite, stilpnomelane, riebekite and minnesotaite) and pyrite (Klein, 2005). The presence of both oxidized and reduced Fe minerals gives BIFs an average oxidation state of $Fe^{2.4+}$ (Klein and Beukes, 1992). The current consensus is that the minerals found in BIFs today are likely not of primary origin but they rather represent a product of diagenetic and metamorphic alteration of the initially deposited minerals (e.g., Konhauser et al., 2017; Rasmussen et al., 2021).

The composition of these precursor mineral phases is highly debated. Some models for BIF deposition consider the potential for precipitation of Fe(II)-containing minerals, including greenalite (Rasmussen et al., 2017, 2021), green rust (Zegeye et al., 2012; Halevy et al., 2017), and magnetite (Li et al., 2017; Thibon et al., 2019) directly from the water column. The common view, however, is that the precursor mineral phase to BIFs consisted of a Fe(III) (oxyhydr)oxide such as ferrihydrite (e.g., Beukes and Gutzmer, 2008; Pecoits et al., 2009; Alibert, 2016; Robbins et al., 2019). BIF deposition has traditionally been explained by the oxidation of Fe^{2+} via O_2 produced by cyanobacteria (Cloud, 1973). Alternatively, another biological mechanism involves anoxygenic photoautotrophic Fe(II)-oxidizing bacteria (photoferrotrophs) that could have driven early primary production by coupling Fe(II) oxidation to CO_2 fixation by harvesting light energy (Hartman, 1984). Konhauser et al. (2002) suggested that this microbial activity could have accounted for most if not all Fe initially deposited in BIFs. Of both biological mechanisms, photoferrotrophy was likely of higher significance for BIF deposition before the GOE. Their adaptation to low light conditions (Kappler et al., 2005) in combination with lower nutrient requirements (Jones et al., 2015; Ozaki et al., 2019) would have given photoferrotrophs a competitive edge over early cyanobacteria. Consequently, as long as the aqueous Fe/PO_4^{3-} stayed above a critical value, photoferrotrophs could have exhausted all upwelling nutrients before they reached the ocean surface water which was likely inhabited by early cyanobacteria (Ozaki et al., 2019), thus marginalizing the role that cyanobacteria played in BIF deposition. Additionally, the early aerial expansion and relevance of early cyanobacteria for BIF deposition might have been halted by Fe(II)-toxicity (Swanner et al., 2015) and high UV fluxes in the upper water column (Mloszewska et al., 2018).

Photoferrotrophs form cell-Fe(III) mineral aggregates (e.g., Posth et al., 2010; Wu et al., 2014) that would have provided an ideal habitat for bacteria able to couple carbon oxidation to Fe(III) reduction (dissimilatory Fe(III) reduction, DIR; Lovley and Phillips, 1986, 1988). This metabolism resulted in the reduction of solid-phase Fe(III) to Fe^{2+} that ultimately would have re-precipitated in the form of secondary Fe minerals such as siderite, magnetite and Fe(II)-silicates which are commonly found in BIFs today. Additionally, the organic carbon utilized during DIR would have been oxidized to inorganic carbon such as

dissolved CO_2 or bicarbonate (HCO_3^-), offering a plausible explanation for the low organic carbon content in BIFs. The significance of microbial Fe(III) reduction for the genesis of BIFs was first hypothesized by Walker (1984) and later further conceptualized by Nealson and Myers (1990). C, O and Fe isotope studies have since stressed the importance of DIR for the post-depositional alteration of BIFs (e.g. Johnson et al., 2003, 2008; Heimann et al., 2010; Steinhoefel et al., 2010; Craddock and Dauphas, 2011; Wang et al., 2015; Teixeira et al., 2017).

Based on the abundance of Fe^{2+} and bicarbonate in the early ocean, it has been suggested that siderite may represent a primary seawater precipitate (e.g., Klein and Beukes, 1989; Kaufman et al., 1990; Steinhoefel et al., 2010; Siahi et al., 2020). However, isotopic studies (e.g., Johnson et al., 2013) and experiments focusing on the precipitation and growth kinetics (e.g., Jiang and Tosca, 2019, 2020) have instead argued against siderite being a primary seawater precipitate. Similarly, petrographic evidence (e.g., Pecoits et al., 2009; Rasmussen et al., 2021) as well as experimental studies (e.g. Lovley, 1991; Zeng and Tice, 2014) suggest that siderite was of secondary or early diagenetic origin, where increased alkalinity as a result of DIR favored its precipitation within the soft sediment (Fischer and Knoll, 2009). Alternatively, siderite could have been formed through the aging of green rust (Halevy et al., 2017) or during low-grade metamorphism (Köhler et al., 2013; Posth et al., 2013; Halama et al., 2016).

Magnetite is formed by adsorption of Fe(II) onto Fe(III) (oxyhydr)oxides and subsequent solid-state conversion (Hansel et al., 2003). Evidence for its formation via DIR is provided by detailed sedimentological and petrographic work which emphasizes an early paragenetic origin of magnetite (e.g. Beukes and Gutzmer, 2008 and references therein, Pecoits et al., 2009), as well as by crystallochemical data suggesting that magnetite crystals contained in BIFs display similarities to modern biogenic magnetite (Li et al., 2011). This has important implications since recent experimental results have cast doubt on a metamorphic origin of magnetite, due to its limited formation under such conditions (Halama et al., 2016). More recent work has emphasized the possibility of magnetite formation through thermal decomposition of siderite at temperatures exceeding 200 °C (Rasmussen and Muhling, 2018), but the significance of this mineral transformation pathway for the least metamorphosed BIFs remains unclear. In contrast, magnetite formed by Fe(III)-reducing bacteria and exposed to metamorphic pressure–temperature conditions exhibited high thermal stability (Li et al., 2013), suggesting its preservation during low-grade metamorphism and thus pointing to a microbial origin for magnetite.

Various Fe(II)-silicates present in BIFs, such as greenalite, chlorite, stilpnomelane, and riebeckite, could also have formed during DIR (Konhauser et al., 2005), although it should be noted that arguments have been made that some minerals such as e.g., greenalite may represent a primary BIF precipitate (see Rasmussen et al., 2021). Those that favor a diagenetic origin suggest that a primary ferrihydrite-Si composite (e.g., Fischer and Knoll, 2009; Alibert, 2016; Reddy et al., 2016; Zheng et al., 2016) and its subsequent reduction during DIR could have led to the release of Fe(II) and Si into sediment pore water. The increase in pore water pH during DIR could have promoted the precipitation of Fe(II)-silicates, thus potentially explaining some of the apparent primary features despite a secondary (diagenetic) origin (Morris, 1993; Pecoits et al., 2009).

In summary, there is strong precedence for the formation of primary cell-Fe(III) mineral aggregates by photoferrotrophs and subsequent diagenetic alteration of these mineral aggregates by DIR during the genesis of BIFs. Konhauser et al. (2005) estimated that up to 70% of the initially deposited Fe(III) might have been reduced microbially and cycled back into the water column, resulting in the formation of secondary biogenic magnetite and siderite (Han et al., 2020) as well as Fe(II)-silicates (Fischer and Knoll, 2009). While both processes are well understood individually, it is unclear if, and how, they might have interacted in the water column during the sedimentation of primary BIF precipitates such as Fe(III) (oxyhydr)oxides. Additionally, it is unknown how the continuous recycling of cell-Fe mineral aggregates within the water column via microbial Fe cycling, i.e., the combination of photoferrotrophy and microbial DIR, would have influenced the evolution of the secondary mineralogy in BIFs and if minerals such as siderite, magnetite and Fe(II)-silicates could already have been formed in the water column. To answer these questions, we conducted experiments simulating the Precambrian ocean chemistry where we co-cultivated marine photoferrotrophs and marine Fe(III)-reducing bacteria. We followed geochemical parameters, mineral identity and composition of cell-mineral aggregates over time and placed our experimental data into the context of BIF deposition by applying simplified calculations regarding the water column residence time of these cell-mineral aggregates.

2. MATERIALS AND METHODS

2.1. Source of microorganisms, culturing medium and growth conditions

Chlorobium sp. strain N1 is a marine photoferrotroph belonging to the green-sulfur bacteria, which was isolated from Norsminde Fjord, Denmark (Laufer et al., 2016, 2017). Its closest relative, with a sequence similarity of 94%, is *C. ferrooxidans* KoFox (Heising et al., 1999). A marine Fe(III)-reducing enrichment culture, which showed a 99% sequence similarity to *Shewanella colwelliana*, was obtained from the same field site (Laufer et al., 2016). Both cultures have been kept in our laboratory culture collection since their isolation.

Both cultures were routinely cultivated on artificial seawater medium (ASW; see Laufer et al., 2016) buffered by 30 mM bicarbonate under a N_2/CO_2 (90:10) headspace. For the current study the pH was set to 7.1 to correspond to that predicted for the Precambrian ocean (Halevy and Bachan, 2017; Krissansen-Totton et al., 2018). Additionally, to obtain Si concentrations covering the range of concentrations assumed for the Precambrian ocean (0.67–

2.2 mM, saturation with respect to cristobalite and amorphous silica, respectively; Siever, 1992; Maliva et al., 2005), 0.19 g L^{-1} and 0.63 g L^{-1} $Na_2SiO_3 \times 9\ H_2O$, respectively, were added. All stock cultures were grown in 250 mL serum bottles containing 100 mL growth medium with; (1) no added Si, (2) low Si or (3) high Si concentrations (see Table 1).

For the cultivation of *Chlorobium* sp. strain N1 the ASW medium was additionally amended with 5 mM Fe(II) (1 M $FeCl_2 \times 4\ H_2O$ stock solution; Hegler et al., 2008). This Fe(II) concentration is approximately one order of magnitude higher than the maximum concentration assumed for the Precambrian ocean by early studies (0.5 mM; Holland, 1973; Morris, 1993) but was necessary to obtain enough solid-phase (Fe) precipitates for analysis. However, two recent studies estimated that Fe(II) concentrations might have been up to several mM (Derry, 2015; Jiang and Tosca, 2019), which is in the range of the concentrations we used. Cultures were incubated at 20 °C in light using a 40-W incandescent light bulb.

Stock cultures of the marine *S. colwelliana* culture were grown routinely on ASW containing either no Si, low Si or high Si, with 5 mM Fe(III) as terminal electron acceptor (TEA) provided as 2-line ferrihydrite (Schwertmann and Cornell, 2008), and 5 mM lactate as electron donor and C source. However, *S. colwelliana* cultures used for the inoculation of the experiments were grown on 20 mM fumarate as TEA and 10 mM lactate as both the electron donor and C source for at least two generations to minimize the amount of Fe transferred to the experiment. All cultures were incubated in the dark at room temperature.

Prior to inoculation, all media amended with Si and/or Fe(II) were placed at 5 °C for > 48 h to maximize the removal of any silicate or Fe(II) carbonate or phosphate (likely siderite or vivianite; Hohmann et al., 2009) which may have formed. Thereafter, the pH was re-adjusted to 7.1 when necessary, the precipitates were removed by sterile filtration (polyethersulfone, 0.22 µm pore size Steritop filter unit, Millipore, Merck KGaA, Darmstadt, Germany) inside an anoxic glovebox (100% N_2 atmosphere) and the headspace was exchanged for N_2/CO_2 (90:10). The extent of Fe(II) and $Si(OH)_4$ removal during filtration of Fe(II)-containing medium used in our experiments, as determined by the ferrozine and molybdenum blue colorimetric assays (see Section 2.3.2), is detailed in Table 1.

2.2. Experimental setup

2.2.1. Preparation of the inoculum

Chlorobium sp. strain N1 was inoculated directly from a stationary phase culture grown on Fe(II) with the respective Si concentration (no, low or high Si; compare Table 1).

For the *S. colwelliana* culture, cultures grown on fumarate and lactate were harvested by centrifugation at 1761 *g* and washed 3 times with a sterile 30 mM bicarbonate buffer to remove any remaining metabolic products. Afterwards, the cultures were resuspended in ASW of the respective Si concentration, made anoxic by flushing with N_2/CO_2 (90:10) and stored at room temperature. The cell suspensions were used within 48 h of preparation.

2.2.2. Microbial Fe cycling experiments

One third of all bottles had no added Si to represent modern ocean Si concentrations, another third contained low concentrations of Si to represent the lower limit of the ancient ocean Si concentrations (0.67 mM), and the last third contained 1.4 mM (high Si) to approximate the upper limit of assumed Si concentrations (Siever, 1992; Maliva et al., 2005). All experiments were run in biotic triplicates with one abiotic control. Recent studies on modern-day analogues for the ancient ocean suggested that the Fe could have been cycled 2–11 times before being removed by sedimentation (Bauer et al., 2020; Roland et al., 2021). Therefore, to remain on the conservative side of these estimates, we performed 3 consecutive microbial Fe cycles, each consisting of an oxidative half cycle (activity of photoferrotrophs in light) and a reductive half cycle (activity of Fe (III)-reducing bacteria in dark), which equaled 58 days in the longest experiment. All experiments were carried out in a temperature range of 20–28 °C. These temperatures are in line with recent studies which cast doubt on a hot (~80 °C) early ocean (e.g., Galili et al., 2019; Liljestrand et al., 2020; Sengupta et al., 2020; Zakharov et al., 2021) and instead suggest a temperate ocean (<50 °C; Krissansen-Totton et al., 2018) with temperatures possibly as low as 26–35 °C (Blake et al., 2010; de Wit and Furnes, 2016).

The first oxidative half cycle was initiated by the addition of 1% inoculum (*v/v*, 1 mL) of *Chlorobium* sp. strain N1 grown on the respective Si concentrations to the biotic triplicates (Fig. 1). Quantification of cell numbers of the *Chlorobium* sp. strain N1 inoculum by flow cytometry was not possible due to poor staining and a high background

Table 1
Extent of Fe(II) and $Si(OH)_4$ removal during filtration of Fe(II)-containing ASW.

Medium	Expected concentration		Final concentration		Loss upon filtration	
	Fe(II) [mM]	$Si(OH)_4$ [mM]	Fe(II) [mM]	$Si(OH)_4$ [mM]	Fe(II) [%]	$Si(OH)_4$ [%]
ASW, no Si	5.00	0.00	4.75	0.00	5.0	0.0
ASW, low Si	5.00	0.67	4.40	0.71	12.0	0.0
ASW, high Si	5.00	2.20	4.23	1.43	15.4	35.0

Values are based on concentrations measured prior to setup of the experiment and inoculation.

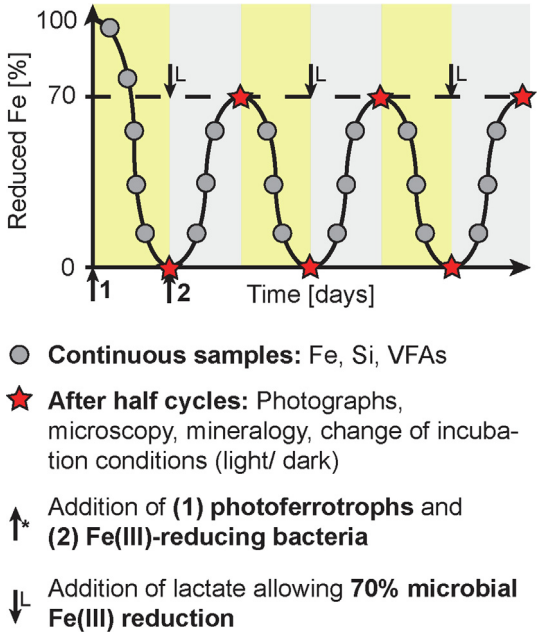

Fig. 1. Overview of experimental setup for the cycling experiments with alternating oxidative and reductive periods and sampling pattern (grey dots and red stars). Yellow shaded areas mark oxidative periods by incubation in light at 20 °C. Grey shaded areas mark reductive periods by incubation in the dark at room temperature.

signal (see Section 2.3.1). Therefore, we estimated the cell number of the inoculum based on Laufer et al. (2017). Those authors used twice the Fe(II) concentration of our experiments (10 mM), which yielded approximately 8×10^8 cells mL^{-1}. Based on this, a total of approximately 4×10^8 cells (4×10^6 cells mL^{-1} in experiment) were added to our experiment. The second and third oxidative half cycle were initiated by transferring the cultures from the dark conditions, under which they were maintained during the reducing half-cycles, to light conditions without addition of new cells (Fig. 1). For the oxidative half cycles, all cultures were incubated at 20 °C in light. Samples were taken prior to inoculation, after inoculation and at regular time intervals during the experiment as described below. The oxidative half cycles were considered finished once > 95% of the initial Fe(II) was oxidized (as determined by the ferrozine assay).

The first reductive half cycle was initiated by the addition of 0.1% inoculum (*v/v*, 0.1 mL) of the *S. colwelliana* culture, which is approximately 1×10^8 cells (based on flow cytometry measurements; 1×10^6 cells mL^{-1} in experiment; Fig. 1). Additionally, lactate was added at a concentration that would theoretically allow for 70% of the Fe(III) to be reduced to Fe(II) (per Konhauser et al., 2005). Based on the initial Fe(II) concentration (4.2–4.8 mM, Table 1), assuming that all Fe(II) was oxidized, the required concentration of lactate was between ~1 and 1.2 mM, depending on the individual experiments. During reductive conditions, all cultures were wrapped in Al foil and incubated at room temperature (ca. 26–28 °C) in the dark. The second and third reductive half cycles were initiated by the addition of lactate to a concentration that again allowed for up to 70% Fe(III) reduction and were transferred to dark conditions. No new cells were added after the first reductive half cycle. Samples were taken prior to and after inoculation and lactate addition and at regular time intervals during the experiment as described in the following section. The reductive half cycles were terminated once approximately 70% Fe(III) reduction had been achieved (determined by ferrozine assay) and the cultures were transferred back to light conditions.

2.2.3. Sampling

All sampling was performed in an anoxic glovebox (100% N_2 atmosphere). Samples for wet geochemistry were taken at regular time intervals (every 2–3 days) throughout the experiments and include samples for Fe concentration and Fe redox speciation, dissolved Si and volatile fatty acids (VFAs, as a measure for metabolic activity of the Fe(III)-reducers). Solid samples, which include those for light and electron microscopy and mineral identification by XRD and ^{57}Fe Moessbauer spectroscopy, were taken at the end of each half cycle (Fig. 1) as detailed below (Sections 2.3.3 and 2.3.4).

2.2.4. Characterization of primary precipitates (formed after first oxidative half-cycle)

For the characterization of primary precipitates (cell-Fe(III) mineral precipitates formed after the first oxidative half-cycle), additional serum bottles (biotic triplicates, no control) were set up as detailed at the beginning of Section 2.2.2 for the oxidative half cycles. Once all Fe(II) was oxidized (> 95%, as determined by the ferrozine assay), the content of all serum bottles was harvested quantitatively and further processed for mineralogy and aggregate size analysis (see below) as well as organic carbon content and surface charge as detailed in supplementary text S1.

2.3. Sample processing and analytical techniques

2.3.1. Cell counts

Cell numbers were determined by flow cytometry (Attune NxT Flow Cytometer, Thermo Fisher Scientific Inc., Waltham, Massachusetts, USA) using 200 µL sample in 96-well plates. Samples for the Fe(III)-reducing cultures were prepared by sequential dilution of a 100 µL sample from the culture with 30 mM bicarbonate buffer (up to 10^{-3}). *Bac*Light™ green bacterial stain (Thermo Fisher Scientific Inc., Waltham, Massachusetts, USA) was added at a concentration of 1 µL mL^{-1} and incubated in the dark for 15 minutes prior to measurement. A detailed description of the various experimental approaches and parameters modified during sample preparation for *Chlorobium* sp. strain N1 is given in the supplementary text S2.

2.3.2. Wet geochemistry

A detailed description of the processing of wet geochemical samples is provided in supplementary text S3. In short, for total Fe quantification (Fe(II) + Fe(III)), a suspension

aliquot was digested in 1 M HCl, which should mostly target short-range ordered Fe minerals. For dissolved Fe and Si as well as VFA quantification, the remaining aliquot was centrifuged and subsamples of the supernatant fixed with 1 M HCl, diluted with Milli-Q® water (Merck KGaA, Darmstadt, Germany), or preserved as is.

2.3.2.1. Fe analysis and calculation of maximum Fe(II) oxidation and Fe(III) reduction rates. Fe concentrations and redox speciation (Fe(II) and Fe(III)) were determined using a modified protocol for the ferrozine assay (Stookey, 1970) as detailed in Hegler et al. (2008). The absorption at 562 nm was measured using a Multiskan GO Microplate Spectrophotometer with internal software (SkanIT RE for Multiskan GO 3.2; Thermo Fisher Scientific Inc., Waltham, Massachusetts, USA). Maximum Fe(II) oxidation and Fe(III) reduction rates of the respective oxidative or reductive half cycles were determined by linear regression analysis through 3 consecutive points at the steepest slope of the total Fe(II) ($Fe(II)_{HCl}$) curve.

2.3.2.2. Si analysis. Quantification of dissolved monomeric Si was performed using a modified protocol of the molybdenum blue method developed by Strickland and Parsons (1972) as detailed in supplementary text S3. 200 µL sample aliquots were transferred into a black-walled micro-titer plate and the absorption measured at 810 nm using a Multiskan GO Microplate Spectrophotometer.

2.3.2.3. High pressure liquid chromatography (HPLC). VFAs were quantified using a Shimadzu prominence (Shimadzu Corp., Kyoto, Japan) HPLC system equipped with a Biorad Aminex HPX87H column with 5 mM H_2SO_4 as eluent and a diode-array detector. The flow rate was set to 0.6 mL min^{-1}.

2.3.3. Microscopy

2.3.3.1. Fluorescence and light microscopy. For light and fluorescent microscopy, approximately 10 µL sample was taken, transferred to a microscope slide and mixed with 1 µL of SYTO® 9 green fluorescent dye (LIVE/DEAD™ *Bac*Light™ Bacterial Viability and Counting Kit, Thermo Fisher Scientific Inc., Waltham, Massachusetts, USA), incubated for 10 minutes in the dark and immediately analyzed. Fluorescence microscopy was performed on fresh samples using a Leica DM5500 epifluorescence microscope (Leica Microsystems GmbH, Wetzlar, Germany) at 40x magnification.

2.3.3.2. Scanning electron microscopy (SEM). Samples for SEM analysis were prepared as detailed in supplementary text S3. SEM imaging for investigation of mineral morphology and cell-mineral associations was performed at the Center for Light-Matter Interaction, Sensors & Analytics (LISA+) at the University of Tuebingen, Germany. Secondary electron (SE) images were obtained using a JEOL JSM-6500F field emission SEM with a Schottky field emitter (JEOL Ltd., Tokyo, Japan). The instrument was operated at an acceleration voltage of 5 kV with a working distance of 10 mm.

SEM imaging for particle size analysis was performed at the Center for Applied Geosciences, University of Tuebingen, Germany. SE imaging was performed using a LEO 1450 VP SEM (Carl Zeiss AG, Oberkochen, Germany) equipped with an Everhart-Thornley SE-Detector. The instrument was operated at an acceleration voltage of 7 kV and a working distance of 8 mm.

2.3.4. Mineral identification

2.3.4.1. ^{57}Fe Moessbauer spectroscopy. Samples for mineral analysis by ^{57}Fe Moessbauer spectroscopy were prepared by filtration onto 0.45 µm filter papers (MF-Millipore™, 0.45 µm MCE membrane, Merck KGaA, Darmstadt, Germany) which were embedded in Kapton tape and stored in anoxic (100% N_2) air-tight bottles at −20 °C until analysis. ^{57}Fe Moessbauer spectroscopy was performed at the Geomicrobiology group, University of Tuebingen as detailed in supplementary text S3.

2.3.4.2. X-ray diffraction (XRD). XRD analysis was conducted at the Soil Chemistry group, ETH Zuerich, Switzerland on the same samples analyzed by ^{57}Fe Moessbauer spectroscopy as detailed in supplementary text S3.

2.3.5. Aggregate size analysis and calculation of settling velocity

Stokes' law was used to calculate the settling velocity of the primary Fe(III) mineral-cell aggregates (aggregates formed during the first oxidative half-cycle). The aggregate size was determined in SEM micrographs by measuring the longest axis for any given aggregate. The aggregates measured were randomized by drawing a vertical, a diagonal and a horizontal line from the top left corner of any given image and measuring all aggregates along those lines. In order to obtain some statistical significance, the size of at least 100 aggregates was determined using the ImageJ software. In case less than 100 aggregates along the vertical, horizontal and diagonal lines were counted, all aggregates were measured. Due to lacking consideration of size variations in z direction by 2D imaging with SEM, the results may be biased. Additional uncertainty may arise due to sample processing, i.e., chemical fixation and sequential dehydration, as this may also alter the size of the cell-Fe mineral aggregates compared to the aggregates present in suspension.

2.3.6. Statistical analyses

All statistical analyses were performed using IBM® SPSS® Statistics Version 26 (IBM Corp., Armong, New York, USA).

3. RESULTS

3.1. Microbial Fe(II) oxidation and Fe(III) reduction under varying Si concentrations

We co-cultivated the marine photoferrotroph *Chlorobium* sp. strain N1 and a marine Fe(III)-reducing enrichment culture of *S. colwelliana* under conditions simulating the proposed geochemistry of an early ocean. In these

experiments, we monitored microbial activity by following changes in dissolved and total Fe, dissolved Si and VFAs.

For the first oxidative half cycle (day 0–18), all three setups showed an initial lag phase of 4 days (Fig. 2A, D and G). Thereafter, the 1 M HCl-extractable total Fe(II) ($Fe(II)_{HCl}$) in all setups was completely oxidized within 10 days. Maximum Fe(II) oxidation rates decreased slightly with increasing Si concentrations (Fig. 3). 1 M HCl-extractable total Fe concentrations (Fe_T, Fe(III) + Fe(II)) showed contrasting trends for different Si concentrations. While the Fe_T concentration decreased from approximately 4.5 mM to 0.5 mM in the Si-free setup (Fig. 2B) and to between 2.0 and 2.5 mM in the low Si setup (Fig. 2E) until day 18, the high Si setup showed (within error) no decrease in Fe_T (Fig. 2H) suggesting that all Fe in the minerals formed was HCl-extractable. Since 1 M HCl dissolves mostly short-range ordered Fe minerals, this suggests an increasing quantity of crystalline Fe(III) minerals with decreasing Si concentration (Fig. 2B, E and H). The Si containing setups showed, concomitant with Fe(II) oxidation, a sharp decrease in dissolved Si (Si_{diss}) concentrations until day 18 (Fig. 2D and G).

Upon completion of the first oxidative half cycle, the biotic triplicates of all setups were inoculated with the Fe(III)-reducing enrichment culture and all bottles (including abiotic, non-inoculated controls) were amended with

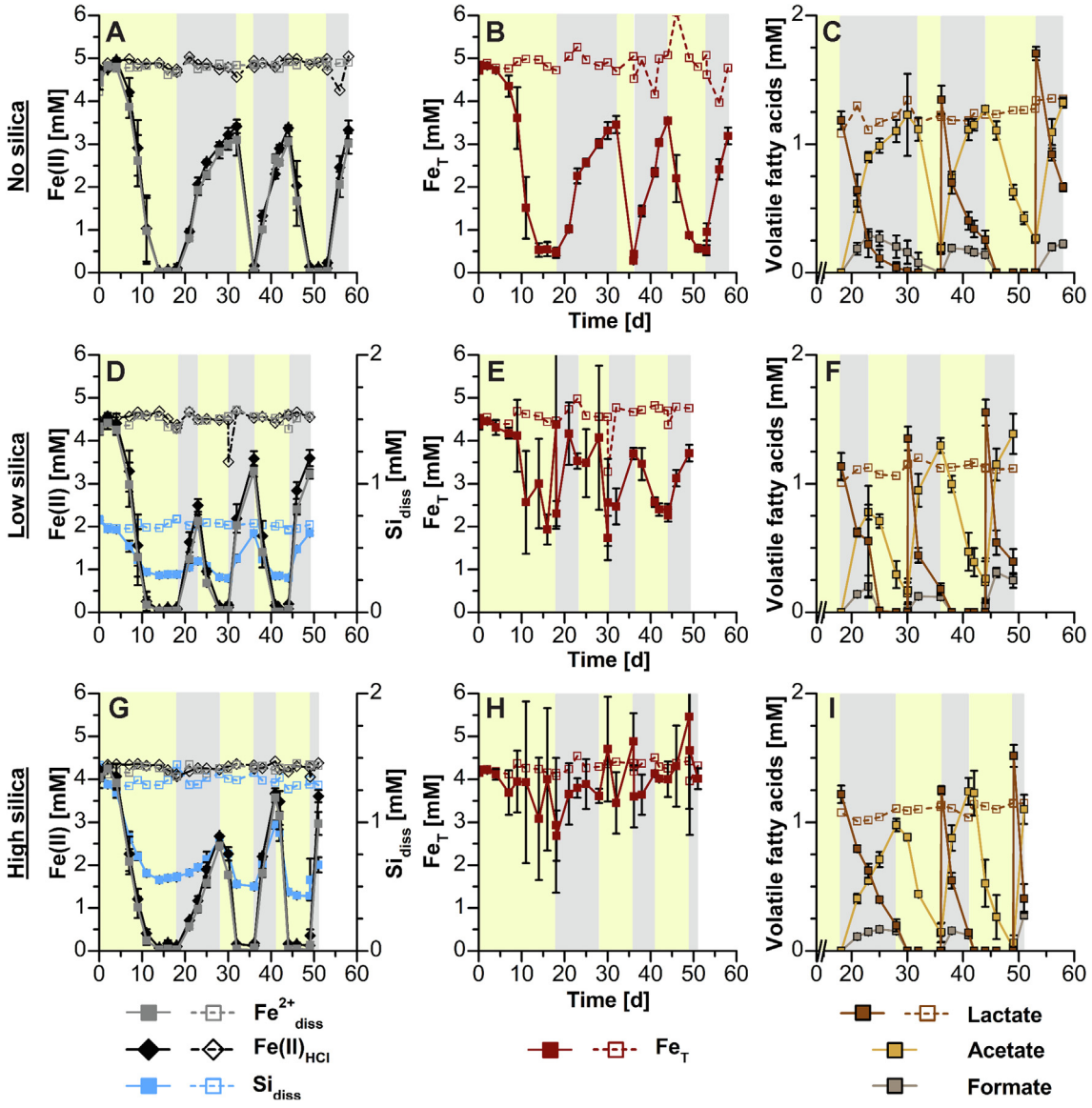

Fig. 2. Variations in wet geochemical parameters (total Fe(II) ($Fe(II)_{HCl}$), dissolved Fe(II) (Fe^{2+}_{diss}), dissolved Si (Si_{diss}), 1 M HCl-extractable total Fe (Fe_T) and volatile fatty acids) over time during microbial Fe cycling experiments. The top row shows the results of the Si-free setup, the middle row results of the low Si setup and the bottom row the results of the high Si setup. Closed symbols with solid lines are biotic triplicates. Open symbols with dashed lines are abiotic controls. Yellow shaded areas mark incubation at 20 °C in light. Grey shaded areas mark incubation at room temperature in dark. Data shown for biotic setups are mean from triplicates ± standard deviation. Abiotic controls are single measurements.

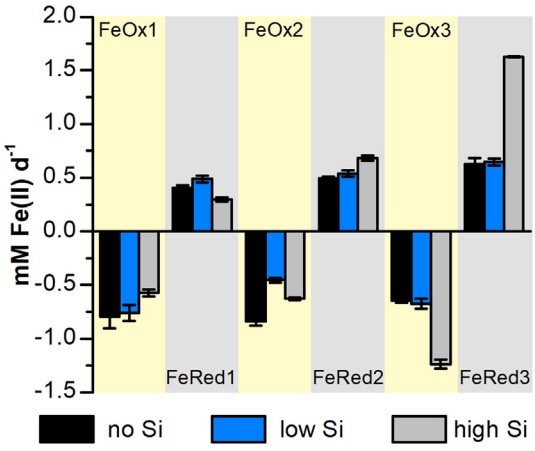

Fig. 3. Maximum Fe(III) reduction (positive values) and Fe(II) oxidation rates (negative values). Rates were determined by linear regression analysis through 3 consecutive points at the steepest slope of the total Fe(II) curve. Values are the mean from biotic triplicates ± standard deviation.

lactate to a concentration that could theoretically allow for 70% of the initially oxidized Fe(II) to be reduced. Fe(III) reduction was initiated by transferring all bottles to the dark. In the Si-free setup > 70% Fe(III) was reduced in 14 days (days 18–32), in the low Si setup around 60% of the Fe(III) was reduced within 5 days (days 18–23), and > 60% in 10 days in the high Si setup (days 18–28; Fig. 2A, D, G). This is partially reflected by the maximum Fe(III) reduction rates, which was the highest for the low Si setup and lowest for the high Si setup (Fig. 3). Similar to the oxidative half cycle, Fe_T depended on the Si concentration. In the no Si setup, it increased considerably, in the low Si setup it increased slightly, while in the high Si setup Fe_T concentrations remained constant (Fig. 2B, E, H). In all cases, over 85% of the Fe(II) formed during microbial Fe(III) reduction was present as dissolved Fe^{2+} (Fe^{2+}_{diss}), suggesting that both the formation of Fe(II)-containing minerals and adsorption of Fe(II) to Fe(III) (oxyhydr)oxides was limited (Fig. 2A, D, G). Microbial Fe(III) reduction was linked to incomplete lactate oxidation and acetate and formate formation (Fig. 2C, F, I). The ratio of Fe(III) reduced to lactate oxidized was below the expected 4:1 ratio (Eq. (1)), ranging from 3.02 ± 0.65 (low Si) to 3.56 ± 0.14 (high Si).

$$4Fe(OH)_3 + C_3H_5O_3^- + 7H^+ \rightarrow Fe^{2+} + C_2H_3O_2^- + HCO_3^- + 10H_2O \quad (1)$$

In the Si-containing setups, dissolution of Fe(III) minerals during microbial Fe(III) reduction resulted in the remobilization of Si immobilized during the previous oxidative half cycle (Fig. 2D and G).

After incubation under dark conditions during the first reductive half cycle, there was no lag phase during Fe(II) oxidation when shifting to the second oxidative half cycle (Fig. 2). Fe(II) oxidation was faster than during the first oxidative half cycle: in the second cycle ≥ 95% $Fe(II)_{HCl}$ was oxidized in 4 days (no Si, high Si) or 5 days (low Si), respectively (Fig. 2A, D, G). This is partially reflected in slightly higher maximum Fe(II) oxidation rates for the no Si and high Si setups, respectively (Fig. 3). Fe_T concentrations followed the same trends as during the first oxidative half cycle (Fig. 2B, E, H). Similar to the first oxidative half cycle, the Si_{diss} concentration decreased during Fe(II) oxidation for both the low Si and high Si setup (Fig. 2D and G). Additionally, in all biotic replicates, formate as well as the remaining lactate were metabolized, while approximately 0.1 mM acetate remained in solution (Fig. 2C, F, I).

Upon completion of the second oxidative half cycle, the second reductive half cycle was initiated by the addition of lactate to the biotic triplicates and transferring all bottles to dark conditions (Fig. 2). The maximum Fe(III) reduction rates increased compared to the first reductive half cycle (Fig. 3), while the Fe_T concentrations followed previously observed trends (Fig. 2B, E, H). Comparable to the first reductive half cycle, > 90% of the Fe(II) formed during microbial Fe(III) reduction was present as Fe^{2+}_{diss} in all setups, whereas the remaining Fe(II) was associated with the solid phase (Fig. 2A, D, G). Similar to the first reductive half cycle, the oxidation of lactate was incomplete, resulting in the formation of acetate and formate (Fig. 2C, F, I). Compared to the first reductive half cycle, the ratio of Fe(III) reduced to lactate oxidized decreased to between 2.74 ± 0.11 (no Si) and 3.18 ± 0.18 (high Si). The microbial reduction of Fe(III) minerals resulted in an extensive release of Si back into solution (Fig. 2D, G).

During the third and last oxidative half cycle, Fe(II) oxidation was fastest in the high Si setup (≥ 95% $Fe(II)_{HCl}$ oxidation within two days) and slower for the no Si and low Si setups with 5 and 6 days, respectively, being required for complete Fe(II) oxidation (Fig. 2A, D, G). This is reflected in the maximum Fe(II) oxidation rates, which showed a sharp increase for the high Si setup and remained constant for the no and low Si setup (Fig. 3). Fe_T and fatty acid concentrations (Fig. 2B, C, E, F, H, I), as well as Si_{diss} concentrations (Fig. 2D, F), followed previously established trends.

The final reductive half cycle was generally the fastest, with 5 days required to recycle ≥ 70% of the previously oxidized $Fe(II)_{HCl}$ by the no and low Si setups and only 2 days required by the high Si setup (Fig. 2A, D, G). This is mirrored by higher maximum Fe(III) reduction rates for all three setups (Fig. 3). Fe_T concentrations followed the trends observed for the first two cycles (Fig. 2B, E, H). As for the first two cycles, Fe(II) was mainly present as Fe^{2+}_{diss} (> 80%). Fe(III) reduction was linked to incomplete lactate oxidation (Fig. 2C, F, I), where the ratio of Fe (III) reduced to lactate oxidized further decreased to on average below 3 for all Si concentrations. During the final reducing half cycle Si_{diss} concentration increased back to final values of 0.62 ± 0.02 mM (start of the experiment 0. 72 ± 0.00 mM) in the low Si setup and 0.67 ± 0.06 mM (start of the experiment 1.40 ± 0.02 mM) in the high Si setup (Fig. 2D, G).

3.1.1. Statistical analysis of wet geochemical results

In order to determine which factors influenced the kinetics of microbial Fe cycling, we performed statistical

analyses on the wet geochemical results. We found that both the number of microbial Fe cycles and the Si concentration had a significant influence on the maximum Fe(II) oxidation and Fe(III) reduction rates.

In summary, all three setups showed faster Fe(II) oxidation and Fe(III) reduction with an increasing number of microbial Fe redox cycles. This is reflected by an overall significant (positive) effect of an increasing number of Fe cycles on the maximum Fe(III) reduction rates (see supplementary text S5). However, the effect of the number of Fe cycles on the maximum Fe(II) oxidation rates was different depending on the presence of Si, and rates either decreased over time (no Si), were not affected (low Si) or increased (high Si; see supplementary text S5).

In contrast to the number of cycles, the effect of Si on maximum Fe(II) oxidation or Fe(III) reduction rates varied depending on the redox cycle: Si did not significantly influence the maximum Fe(II) oxidation rates during the first oxidative half cycle, and it appeared to have a negative effect during first reductive half cycle if present at high concentrations (one-way ANOVA, $F = 31.737$, $df = 2, 6$, $P = 0.001$, Tukey HSD post-hoc test, $\alpha = 0.05$; see supplementary text S5). By the second reductive half cycle, this effect was inverted and high Si concentrations resulted in significantly higher maximum oxidation and reduction rates throughout the remaining experiment compared to the no Si and low Si setups (see supplementary text S5).

Finally, we tested if repeated microbial Fe cycling, in turn, would result in changes in the dissolved Si concentrations. We found a significant decrease in dissolved Si in both the low Si setup (paired t-test, $t = 10.961$, $df = 2$, $P = 0.008$) and high Si setup (paired t-test, $t = 19.282$, $df = 2$, $P = 0.003$): $14.0 \pm 2.2\%$ and $52.2 \pm 4.4\%$ of the initially present dissolved Si, 0.72 ± 0.00 mM and 1.40 ± 0.02 mM, respectively, were removed from solution over the course of microbial Fe cycling.

3.2. Characterization of the cell-mineral aggregates (trans)formed during microbial Fe cycling

In order to determine the Fe mineralogy, the extent and type of cell-mineral associations during microbial Fe cycling, as well as the size and morphology of cell-mineral-aggregates formed, we performed ^{57}Fe Moessbauer spectroscopy and XRD analysis supported by fluorescence microscopy and SEM analysis on samples obtained at the end of each individual half cycle.

3.2.1. Mineral (trans)formation during microbial Fe cycling

After the first oxidative half cycle, Moessbauer analyses identified three mineral phases in the setup without Si. A narrow paramagnetic doublet with an isomer shift (δ) of 0.44 mm s^{-1} and quadrupole splitting (ΔE_Q) of 0.69 mm s^{-1} suggested the presence of a short-range ordered (SRO) Fe(III) (oxyhydr)oxide, which accounted for 13.8% of the spectral area. This doublet could either represent a single mineral entity, such as ferrihydrite (Murad and Schwertmann, 1980; Eickhoff et al., 2014), or a complex mixture consisting of a continuum of ferrihydrite, akageneite and/ or lepidocrocite (Laufer et al., 2017). The magnetically ordered component of the Moessbauer spectrum was dominated by goethite (48.2% of the spectral area) as identified by its hyperfine parameters (supplementary text S4, Pantke et al., 2012). However, in order to obtain an optimal fit, a second magnetically ordered component in the form of collapsed sextet (poorly ordered magnetic component) was required. This collapsed sextet is suggestive of a highly structurally distorted, poorly crystalline mineral phase (Eusterhues et al., 2008; Chen and Thompson, 2018; Fig. 4A and B). The presence of goethite was confirmed by XRD, but no other crystalline Fe mineral phases were detected. By contrast, the Moessbauer spectra of the low Si and high Si setups both consisted of a single narrow paramagnetic doublet with hyperfine parameters suggestive of ferrihydrite (Fig. 4E and H, supplementary text S4; Murad and Schwertmann, 1980; Eickhoff et al., 2014; Gauger et al., 2016). Compared to the Si-free setup, the higher quadrupole splitting of 0.84 mm s^{-1} and 0.86 mm s^{-1} for the low Si and high Si setup, respectively, are suggestive of decreased crystallinity (Murad, 1996; Murad et al., 1988). This is probably due to inhibited particle growth and increased structural strain/disorder in the ferrihydrite particles due to co-precipitated silica (Cismasu et al., 2011, 2014; Eickhoff et al., 2014). No crystalline Fe mineral phases were detected by XRD (Fig. 4F and I).

After the first reductive half cycle, the mineralogy in the Si-free setup was dominated by goethite (91.3%, magnetically ordered sextet, Fig. 4B, supplementary text S4, Dippon et al., 2015). A second mineral phase, whose narrow paramagnetic doublet is suggestive of a SRO Fe(III) mineral like ferrihydrite (Fig. 4B, supplementary text S4; Shimizu et al., 2013; Dippon et al., 2015), accounted for 8.7% of the spectral area. The formation of goethite was independently confirmed by XRD analysis (Fig. 4C). In addition to goethite, XRD analysis suggested the presence of a second, unknown, layered Fe(II) mineral phase, potentially a variety of green rust (Fig. 4C; supplementary text S6; e.g., Hansen, 1989; Simon et al., 2003). The low Si setup was dominated by a poorly ordered magnetic component (>50%), which, based on its hyperfine parameters, was likely a structurally distorted, nano-sized Fe(III) mineral phase that had not undergone complete magnetic ordering (Fig. 4D and E, supplementary text S4; Eusterhues et al., 2008; Chen and Thompson, 2018). However, due to the generally poor signal-to-noise ratio of the Moessbauer spectra, likely due to a high amount of co-precipitated organics, the interpretation remained inconclusive. Additionally, microbial Fe(III) reduction resulted in the formation of some goethite (17.2%, clearly defined sextet, Fig. 4D and E, supplementary text S4) and a SRO Fe(III) mineral phase, likely ferrihydrite (narrow paramagnetic doublet, Fig. 4D and E, supplementary text S4; Shimizu et al., 2013; Dippon et al., 2015). The presence of goethite was confirmed by XRD, but no other crystalline Fe mineral phases were detected (Fig. 4F). In the high Si setup, no formation of any crystalline Fe mineral phases was observed. The Moessbauer spectrum consisted of two paramagnetic doublets. The narrow paramagnetic doublet suggested the presence of a SRO Fe(III) mineral phase, e.g. ferrihydrite, while the wide paramagnetic doublet, which accounted

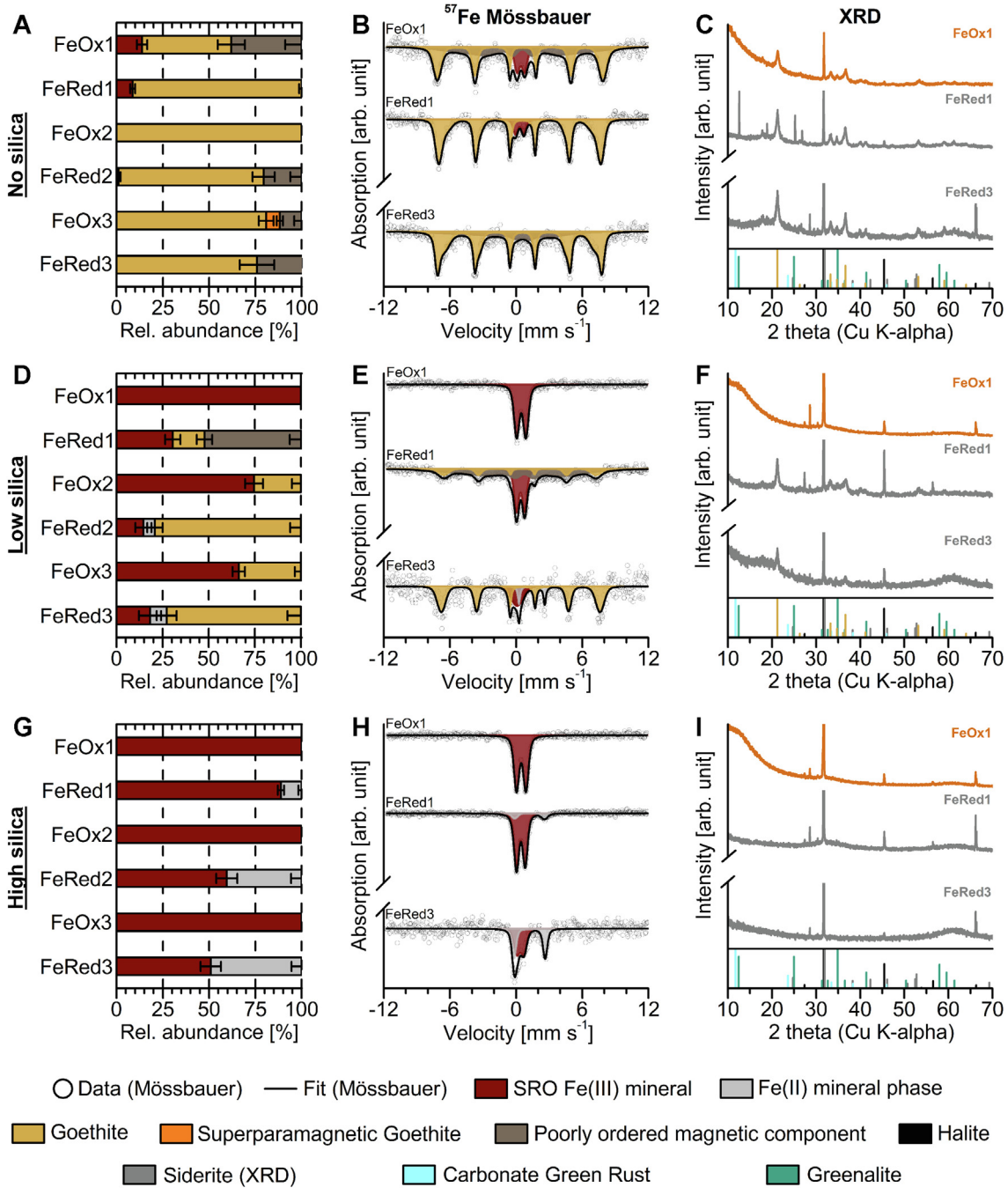

Fig. 4. Relative Fe mineral abundance (based on ^{57}Fe Moessbauer analysis), ^{57}Fe Moessbauer spectra and X-ray diffractograms of mineral products taken at the end of the oxidative and reductive half cycles. Panels A-C show selected results of the no Si setup, D-F results of the low Si setup and G-I results of the high Si setup. Error bars in the relative mineral abundances are based on the error of the relative abundance in the Moessbauer fit. Orange colors in the X-ray diffractograms mark mineral products of oxidative half cycles. Grey colors mark mineral products of the reductive half cycles. The relative intensity of the individual X-ray diffractograms was chosen in order to truncate the major halite reflections and put more emphasis on the changes in the Fe mineralogy. Reflex positions are taken for pure mineral phases. Reference patterns were derived from the ICSD (e.g., Bergerhoff et al., 1987; Zagorac et al., 2019) and AMCSD (Downs and Hall-Wallace, 2003) databases as well as from Hansen (1989) and Simon et al. (2003). Respective CIF file numbers are reported in supplementary text S3, Section 3.2. In addition to the reference diffractogram for carbonate green rust displayed here, reference diffractograms for chloride and sulfate green rust are displayed in supplementary text S6, Figure S4.

for approximately 10% of the spectral area, had hyperfine parameters ($\delta = 1.23$ mm s^{-1} and $\Delta E_Q = 2.70$ mm s^{-1}) suggestive of a Fe(II) mineral phase (Fig. 4G and H, Murad, 2010). Specifically, the Moessbauer hyperfine parameters are indicative of a Fe(II)-silicate, potentially a phyllosilicate (Amthauer and Rossman, 1984; Pollak and Stevens, 1986),

which may have formed through the reaction of Fe^{2+} and Si present in our growth medium. However, it was not possible to independently confirm these results with XRD, suggesting that the precipitate was poorly crystalline in nature. Another putative Fe(II) mineral phase based on elevated Fe^{2+} and bicarbonate concentrations is siderite. However, based on ^{57}Fe Moessbauer spectroscopy we were not able to identify siderite. Furthermore, high halite concentrations in our samples prevented an unambiguous identification of siderite by XRD due to the proximity of major reflections of halite (d-spacing = 2.82 Å, ca. 31.7°2 theta; ICSD 181148, Fig. S4) and siderite (d-spacing = 2.79 Å, ca. 32.0°2 theta; ICSD 169789, Fig. S4).

Both increasing the number of microbial Fe redox cycles and Si concentration seemed to have influenced the mineral crystallinity. Following the first microbial Fe cycle, Moessbauer spectra of the Si-free setup were generally fully magnetically ordered (sextets) and the mineralogy was dominated by goethite; this was independently confirmed by XRD (supplementary text S4, Fig. 4A-C, Fig. S3A and B). However, in order to achieve an optimal fit, the sextet describing goethite in the Moessbauer spectra required an additional component. This indicates that mineral growth and structural ordering were partially restricted, probably by co-precipitated organics. The amount of goethite was higher during the oxidative half cycles (80–100%) than during the reductive half cycles (~75%; Fig. 4A). The remaining up to 25% consisted of the previously described poorly ordered magnetic component of putative nano-crystalline nature (Fig. 4A).

In contrast to the setup without Si, the Moessbauer spectra of the low Si setup generally consisted of a mixture of paramagnetic doublets (SRO Fe(III) and Fe(II) minerals) and a magnetically ordered sextet (goethite), with the latter becoming more abundant over time. Over the course of three consecutive microbial Fe cycles, the amount of goethite formed increased (Fig. 4D-E, Fig. S3C and D) and was higher during reductive compared to oxidative half cycles. During oxidative half cycles, the amount of goethite formed ranged from 25.4% to 33.7%. During the reductive half cycles, it increased from initially 17.2% to 72.8% at the end of the third reductive half cycle. The higher amount of goethite present during the reductive half cycles suggests that the SRO Fe(III) mineral phase was preferentially reduced during microbial Fe(III) reduction. A decrease in the quadrupole splitting value and an increase in the mean magnetic hyperfine field parameter suggest increased structural ordering of both the SRO Fe(III) mineral phase and goethite over time, respectively (supplementary text S4, Fig. S5). However, the mean magnetic hyperfine field value of the goethite formed in the presence of Si was lower than for the goethite formed in the absence of Si (Fig. S5B and D), thus suggesting lower structural ordering of the former. In addition to goethite, a Fe(II) mineral phase was formed during microbial Fe(III) reduction in increasing quantities (6.2% during the second, 9.0% during the third reductive half cycle; Fig. 4D and E, Fig. S3C). As previously explained, clear identification of the Fe(II) mineral phase was difficult. While based on solution geochemistry both the formation of siderite and/or a Fe(II)-silicate are feasible, our observed Moessbauer hyperfine parameters (supplementary text S4) suggest closer similarity of the Fe(II) mineral phase to an Fe(II)-silicate (Amthauer and Rossman, 1984; Pollak and Stevens, 1986). Based on XRD this likely was a layered Fe(II) mineral phase, either a variety of green rust or greenalite (Fig. S3D, Fig. S4).

Finally, the high Si setup showed no changes in mineral crystallinity over three consecutive microbial redox cycles and the mineral product of both oxidative and reductive half cycles remained X-ray amorphous (Fig. 4I, Fig. S3F). The Fe(III) mineral phase consisted entirely of SRO Fe(III) minerals, while a clear identification of the Fe(II) mineral phase was not possible (either siderite and/or an Fe(II) silicate) although Moessbauer hyperfine parameters suggest closer similarity of the Fe(II) mineral phase with a Fe(II)-silicate rather than siderite (Amthauer and Rossman, 1984; Pollak and Stevens, 1986; Fig. 4G and H, Fig. S3E). The amount of Fe(II) minerals increased over time from 11.2% at the end of the first reductive half cycle to 49.1% at the end of the third reductive half cycle (Fig. 4G). Although the mineral products remained X-ray amorphous, a decrease in the isomer shift and quadrupole splitting values of the SRO Fe(III) minerals suggests that they had undergone some degree of structural ordering/increase in crystallinity (Murad et al., 1988; Murad, 1996) over time (Fig. S5A and C).

3.2.2. Macroscopic appearance of cell-mineral aggregates

Overall, visual observations support the previously described mineralogical results. During oxidative half cycles, minerals formed were orange in color and flocculated into cell-Fe(III) mineral aggregates which could be distinguished from each other by eye (Fig. 5A-C, G-I, Fig. S6). The minerals formed during oxidative half cycles in the low Si and high Si setups were of bright orange color throughout the experiment (Fig. 5I & H). By contrast, the minerals formed in the Si-free setup changed from a bright orange (suggestive of a SRO Fe(III) mineral phase) to a dark yellow or ochre at the end of the third oxidative half cycle (suggestive of goethite or lepidocrocite, Fig. 5G-H; Schwertmann and Cornell, 2008). The minerals formed during reductive half cycles were dark brown or black (Fig. 5-D-F, J-L). Although the dark brown to black color of the minerals formed was indicative of the presence of mixed-valent Fe minerals such as magnetite, they were not magnetic (i.e., not attracted by a magnet; see Fig. 5D-F, J-L, Fig. S6).

Generally, the size of the aggregates formed in all three setups seemed to have decreased over several microbial Fe cycles and cell-Fe mineral aggregates present at the end of the experiment were finely dispersed with little flocculation (Fig. 5G-I).

3.2.3. Cell-mineral associations – fluorescence and light microscopy

Overall, there was a close association between cells and minerals during oxidative half cycles (Fig. 5A-C, G-I, Fig. S6), while there were less cells associated with the Fe minerals and more free cells present during reductive half cycles (Fig. 5D-F, J-L). Based on the fluorescence micro-

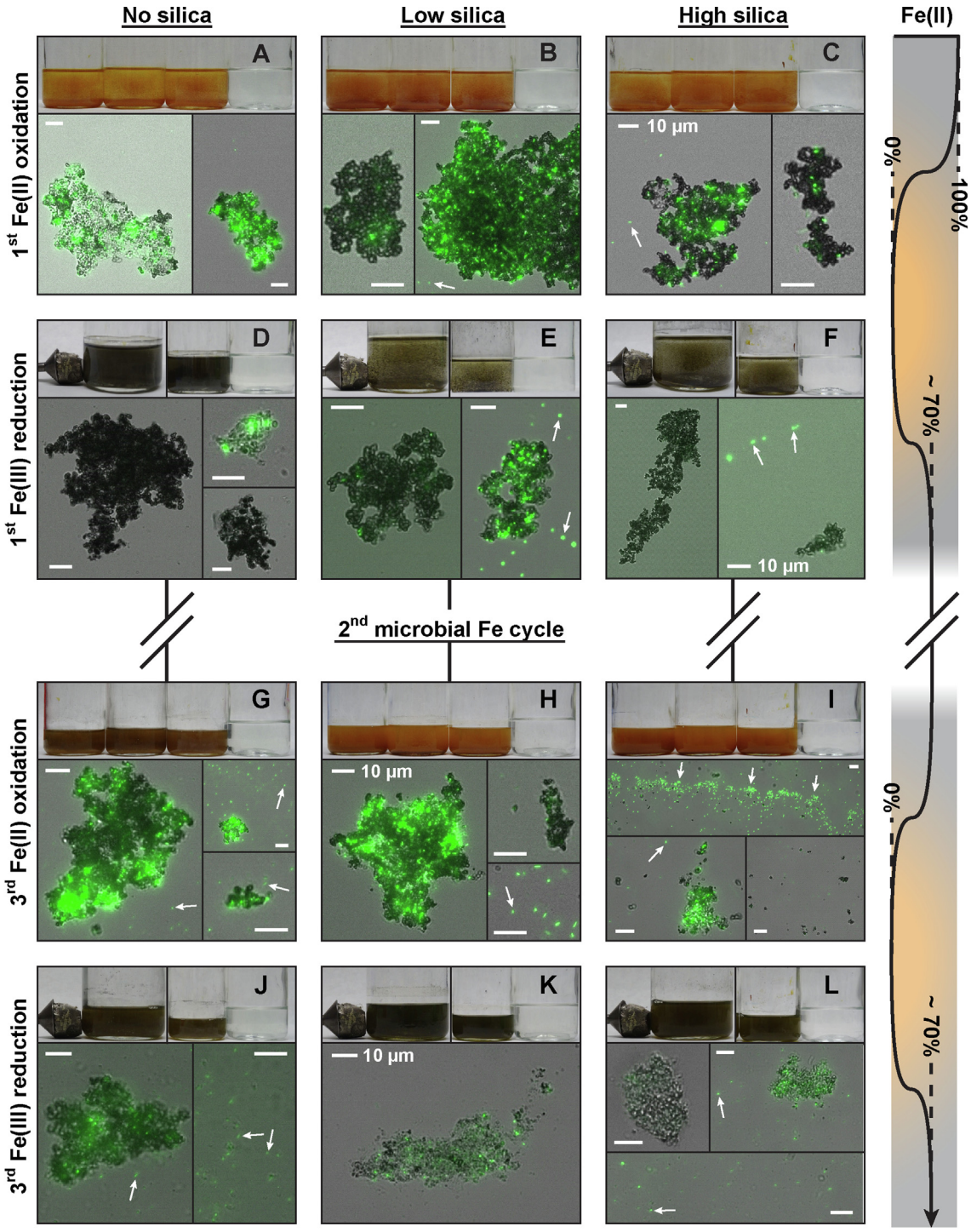

Fig. 5. Overlay of fluorescence and light microscopy images showing cells (green) and mineral particles (dark) over the course of three microbial Fe cycles. The different panels show oxidative half cycles (A-C, G-I) and reducing half cycles (D-F, J-L) for Si-free (first column), low Si (second column) and high Si (last column) setups. Orange colors mark oxidizing conditions, grey colors reducing conditions. The magnet in panels D-F and J-L was placed next to the bottles in order to test for the presence of magnetic minerals like magnetite. All scale bars are 10 µm. Full-size photomicrographs are provided in Appendix B. Supplementary data.

scopy conducted, the overall cell densities appear to have increased over three consecutive microbial Fe cycles, resulting in both a higher number of mineral-associated and free cells during the last microbial Fe cycle (Fig. 5G-L).

In addition to the number of Fe cycles, Si also seemed to influence the extent to which cells were associated with the Fe minerals. Overall, the low Si setup showed the greatest extent of cell-mineral associations throughout the experiment and the lowest number of free cells (Fig. 5B, E, H,

K, Fig. S6). The extent of cell-mineral association in the Si-free setup seemed to be slightly less pronounced or comparable to the low Si setup, but there appeared to be a higher number of free cells during the last microbial Fe cycle (oxidative and reductive half cycle) (Fig. 5G and J). By contrast, the high Si setup showed the lowest extent of cell-mineral associations over all three microbial Fe cycles (Fig. 5C, F, I, L, Fig. S6). Interestingly, the high Si setup seemed to form biofilm like structures after the second oxidative half cycle, which were initially attached to the mineral precipitates formed but were easily suspended upon shaking. These biofilms were marked by a dense network of minerals, accumulation of cells and association of the minerals with the cells under the microscope (Fig. 5I, Fig. S6C).

3.2.4. Morphology and size of cell-mineral aggregates – scanning electron microscopy (SEM)

SEM analysis confirmed the trends observed by fluorescence microscopy. There was generally a close association between cells and minerals during oxidative half cycles and comparatively few cells associated with the minerals during reductive half cycles (Fig. 6, Fig. S7). Furthermore, cell numbers increased over time (Fig. 6, Fig. S7) where the number of cells associated with minerals appeared to be lowest in the high Si setup (Fig. 6C, F, I, L, Fig. S7) and highest in the low Si setup (Fig. 6B, E, H, K, Fig. S7). There were slight differences in cell morphology, with photoferrotrophs being smaller (~1 μm) and bean-shaped (e.g. Fig. 6A-C) whereas Fe(III)-reducers were longer (1.5–2 μm) and rod-shaped (e.g. inset Fig. 6D, number 1, inset Fig. S7D, number 1). Initially, all cell surfaces seemed to be free mineral precipitates (Fig. 6A-F, Fig. S7A-C). However, after the second reducing half cycle there were some cells with surface precipitates (Fig. 6J) or completely entombed in mineral precipitates (Fig. 6I, Fig. S7F).

The mineral morphology showed distinct differences depending on the Si concentration and number of microbial Fe cycles. In the absence of Si, the minerals initially formed during the first oxidative half cycle either had no clear structure (Fig. 6A) or a needle- or platelet-like appearance (inset Fig. 6A, number 2). In the Si-containing setups, the aggregates seemed to consist of spheres of various sizes with a relatively uniform surface structure (approximately 0.5–2 μm diameter; Fig. 6A-C; see also Gauger et al., 2016), some of which appeared to be hollow (inset Fig. 6C, H, J, number 4, Fig. S7C and E) or attached to each other by fibrous structures, probably exopolysaccharides (top inset, Fig. 6B, L, number 3, Fig. S7B and C; Wu et al., 2014). These observations are consistent with the high content in organic compounds previously postulated in the interpretation of our Moessbauer results.

During the following reductive half cycle, the aggregates formed in the Si-free setup were dominated by needle- or platelet-shaped minerals while the aggregates in the Si-containing setups retained their spherical structure (Fig. 6-D-F). However, the spheres in the low Si setup seemed to have a rougher surface compared to the oxidative half cycle (Fig. 6E) and could be separated into two size categories being either 0.5–2.0 μm in size or smaller than 0.2 μm. Over time the no Si setup showed an increasing amount of needle- or platelet-shaped minerals (Fig. 6G, Fig. S7A and D) or cauliflower-like appearance of the spheres formed. In the low Si setup, minerals underwent a similar trend, with spheres equally showing increasing surface roughness (Fig. 6H and K, Fig. S7B and E) and occasionally platelet-like structures (Fig. 6K, number 2), based on XRD and Moessbauer spectroscopy suggesting an increase in mineral crystallinity. The minerals formed in the high Si setup did not undergo any changes over time and generally consisted of relatively smooth spheres (Fig. 6I and L, Fig. S7C and F).

3.3. Size and sedimentation rate of primary cell-Fe(III) mineral aggregates

The mean aggregate size for the Si-free aggregates formed after the first oxidative half cycle was 30.45 ± 21.56 μm. The aggregates formed in the low Si and high Si setups were both significantly smaller (one-way ANOVA, $F = 15.233$, $df = 2, 329$, $P < 0.001$, Tamhane post-hoc test, $\alpha = 0.05$) with 17.90 ± 16.40 μm and 16.01 ± 12.72 μm, respectively (for all setups see supplementary text S1, Fig. S2 for size distribution). Based on these values we calculated the sedimentation rate by applying Stokes' law (Eq. (2)),

$$v_p = \frac{2}{9} \times \frac{r^2 \times g \times (\rho_p - \rho_f)}{\mu} \quad (2)$$

where v_p [m s^{-1}] is the terminal velocity, r [m] is the radius of the particle, g [m s^{-2}] is the gravitational force, ρ_p [kg m^{-3}] the density of the particle, ρ_f [kg m^{-3}] the density of the fluid and μ [kg m^{-1} s^{-1}] the dynamic viscosity of the fluid. Stokes' law is best applied to spherical particles with limited validity for the irregularly shaped cell-Fe(III) mineral aggregates formed in our experiments. Therefore, in order to account for this limitation, we also consider recent results of a study by Li et al. (2021). Li et al. performed *in-situ* measurements of the sedimentation velocity of cyanobacteria-ferrihydrite aggregates, showing that the actual sedimentation velocity was up to 30% slower than estimates based on Stokes' law. Particle densities in our study were assigned based on the previous work of Posth et al. (2010). Although the Si-free aggregates showed the highest organic carbon content (see supplementary text S1) and would thus be estimated to have the lowest density, we also considered the Si-co-precipitation during Fe(III) mineral formation. Based on Posth et al. (2010) we therefore used a density of 2.4 g cm^{-3} for the Si-free aggregates, a density of 2.2 g cm^{-3} for the low Si aggregates and a density of 2.0 g cm^{-3} for the high Si aggregates. Sedimentation rates corrected as per Li et al. (2021) were 2.41 ± 3.28 m h^{-1} for the Si-free, 0.87 ± 1.65 m h^{-1} for the low Si and 0.51 ± 1.05 m h^{-1} for the high Si cell-Fe(III) mineral aggregates (see supplementary text S9 for complete calculations and Fig. S8 for distribution of sedimentation velocities). *Note:* All calculations here are based number-averaged values derived from SEM analysis rather than mass-averaged aggregate sizes. The use of mass-averaged values instead of number-averaged values would result in faster sedimen-

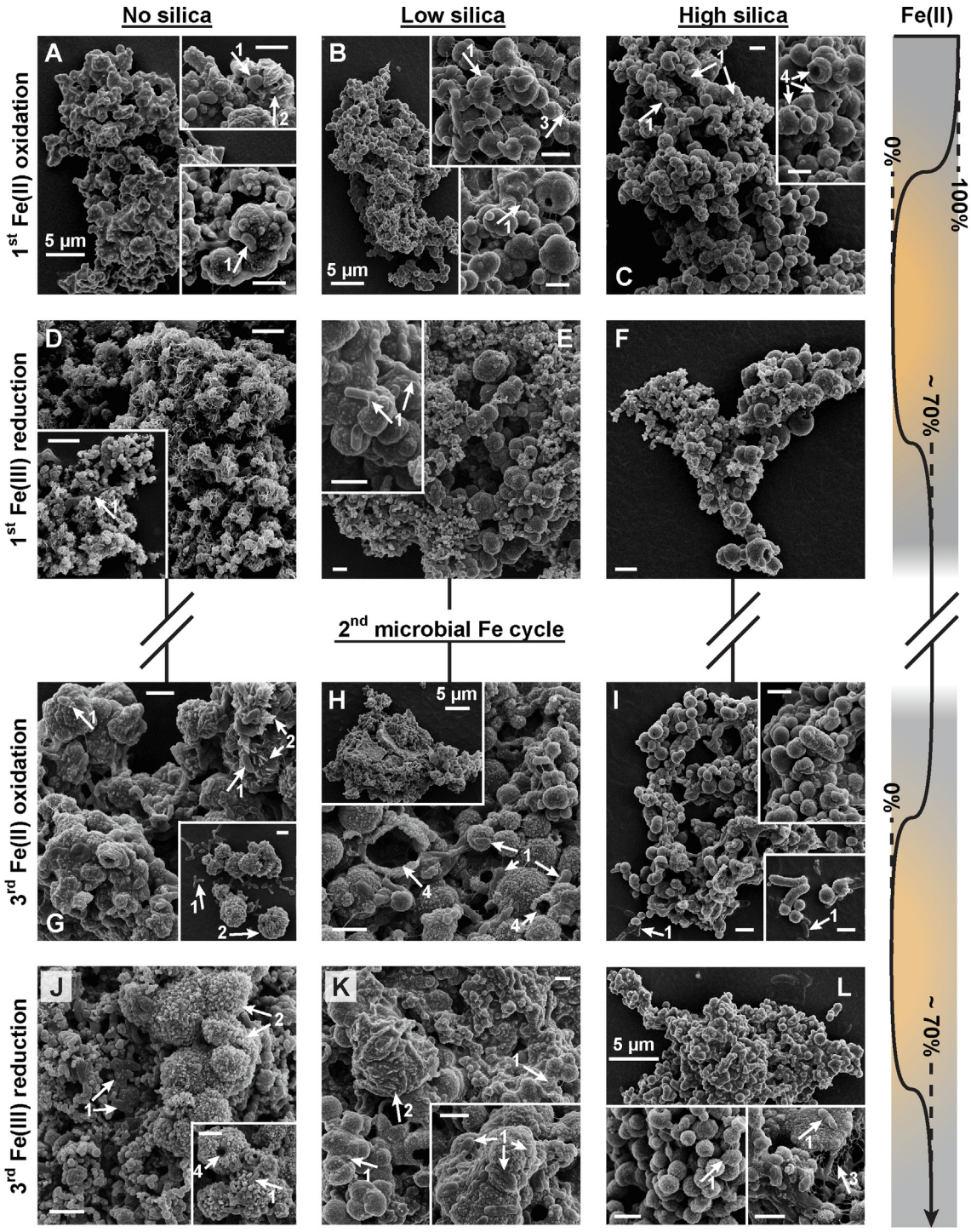

Fig. 6. SEM micrographs of cell-mineral aggregates formed during alternating oxidative and reductive half cycles. The different panels show oxidative half cycles (A-C, G-I) and reducing half cycles (D-F, J-L) for Si-free (first column), low Si (second column) and high Si (last column) setups. Orange colors mark oxidizing conditions, grey colors reducing conditions. Arrows labelled with number 1 indicate cells, arrows labelled with 2 more crystalline parts of the cell-mineral aggregates, arrows labelled with number 3 remains of putative exopolysaccharides and arrows labelled with number 4 hollow mineral spheres. Unless stated otherwise all scale bars are 1 µm. Full-size photomicrographs are provided in Appendix B. Supplementary data.

tation velocities for the bigger particles, whereas the smaller particles would potentially have a much lower sedimentation velocity. Additionally, both the use of 2D imaging techniques and chemical fixation of SEM samples likely resulted in some bias in the results. They should thus be seen as conservative estimates.

4. DISCUSSION

4.1. Interaction between photoferrotrophs and Fe(III)-reducers during microbial Fe cycling

Although the individual influence of photoferrotrophs and Fe(III)-reducing bacteria on the deposition and mineralogy of BIFs has been studied in great detail, their combined influence and the metabolic interaction between both remains unexplored so far. Therefore, one of the major questions driving our study was how photoferrotrophs and Fe(III)-reducing bacteria would have interacted during microbial Fe cycling in the water column of an early ocean.

4.1.1. Fe(II) oxidation by Chlorobium sp. N1 under simulated early ocean conditions

During oxidative half cycles the maximum Fe(II) oxidation rates we observed in all of our setups (between 0.46 ± 0.02 mM d^{-1} and 1.22 ± 0.04 mM d^{-1}) were within the range of published Fe(II) oxidation rates for photoferrotrophs (0.1–4.5 mM d^{-1}; Straub et al., 1999; Kappler and Newman, 2004; Jiao et al., 2005; Hegler et al., 2008; Wu et al., 2014; Gauger et al., 2016; Laufer et al., 2017; Peng et al., 2019) and within the metabolic capability of our strain used (max. rate 0.77 mM Fe(II) d^{-1}; Laufer et al., 2017). However, there was a pronounced effect of the Si concentration on the development of maximum Fe(II) oxidation rates over time. Due to the similar increase in cell numbers in all three setups (no, low and high Si) over time (Fig. 5), changes in cell numbers offer no explanation for the differences in Fe(II) oxidation rates in the three different setups. Fe(II) oxidation rates likely remained stable or decreased in the absence of Si and at low Si concentrations (Fig. 3), due to the simultaneous activity of Fe(II)-oxidizing and Fe(III)-reducing bacteria as suggested by the simultaneous consumption of all substrates (Fe(II) and VFAs, Fig. 1). By contrast, the maximum Fe(II) oxidation rate increased significantly over three microbial Fe cycles in the presence of high concentrations of Si (Fig. 3). Two permissible explanations are (1) the high concentration of Si in the high Si setup and (2) the observed formation of biofilm-like structures in the high Si setup.

Studies by Gauger et al. (2016) and Wu et al. (2017) both observed enhanced Fe(II) oxidation rates in the presence of dissolved Si. Gauger et al. (2016) attributed this to a Fe(II)-toxicity-mitigating effect, caused by high light and Fe(II) concentrations, due to changes in Fe complexation and speciation in the presence of Si. No acceleration of Fe(II) oxidation was observed in our low Si setup compared to the no Si setup, thus suggesting that this effect may be concentration dependent. However, it remains unresolved why this Si effect was only observed during the last oxidative half cycle in the high Si setup. Alternatively, a recent study by Peng et al. (2019) observed that the complexation of Fe(II) by organic compounds resulted in faster Fe(II) oxidation by photoferrotrophs compared to non-complexed Fe(II). They attributed this to higher bioavailability of Fe(II)-organic matter complexes due to lower chemical activation energy and enhanced interaction between Fe(II)-organic matter complexes and c-type cytochromes responsible for Fe(II) oxidation. Another hypothesis put forward by Peng et al. (2019) was the added physiological benefit of oxidizing complexed Fe(II). The oxidation of Fe(II)-organic matter complexes should result in the formation of soluble Fe(III)-organic matter complexes which would thus preclude the necessity of producing Fe(III)-binding ligands or investing in mechanisms to prevent encrustation with Fe(III) minerals. Given the presence of biofilm-like structures (including exopolysaccharides) in the high Si setup following the second oxidative half cycle (Fig. 5, Fig. 6, Fig. S6), these polymeric and complicated organic biomolecules (not fatty acids) could have complexed Fe(II). This potentially explains the higher Fe(II) oxidation rates in the later Fe(II) oxidation cycle.

4.1.2. Microbial Fe(III) reduction under simulated early ocean conditions

In contrast to the oxidizing half cycles, the maximum Fe(III) reduction rates during the reductive half cycles showed a continuous increase for all three setups over three microbial Fe cycles. The overall rates were the lowest for the no Si setup and the highest for the high Si setup.

The continuous increase of the maximum Fe(III) reduction rates is best explained by the perceived increase in cell numbers over time (Fig. 5). The increase in cell numbers is further supported by a consistent deviation of the reaction stoichiometry for microbial Fe(III) reduction from the expected ratio of 4:1 of Fe(III) reduced to lactate oxidized, which ranged from 3.56 ± 0.14 to 2.74 ± 0.11 (compare also Roden and Zachara, 1996), which we attribute to the assimilation of organic carbon in the form of VFAs into cell biomass. Additionally, increasing maximum Fe(III) reduction rates with increasing Si concentrations can best be explained by the decreasing mineral crystallinity with increasing concentrations of Si (Fig. 4). SRO Fe(III) mineral phases have been shown to be more readily accessible by Fe(III)-reducing bacteria compared to more crystalline Fe(III) minerals such as goethite (Postma, 1993; Roden and Zachara, 1996; Roden, 2003; Bonneville et al., 2009). Additionally, Kukkadapu et al. (2004) found that Si-substitution in ferrihydrite enhanced rates and extent of microbial Fe(III) reduction in comparison to Si-free ferrihydrite.

However, similar to the last oxidative half cycle, the maximum Fe(III) reduction rate of the high Si setup was significantly higher during the last reductive half cycle compared to the no and low Si setups (Fig. 3). In this regard a study by Percak-Dennett et al. (2011) showed that Fe(III)-oxide-silica co-precipitates are highly reducible (approximately 80% reduction) under conditions similar to our experiments. This is in contrast to other studies which found that Si incorporation might stabilize ferrihydrite against reductive dissolution and transformation thereby limiting bioavailability (Cismasu et al., 2014). On the one hand, this could be, similar to Fe(II), due to Si partially blocking or reducing the availability of reactive surface sites (Roden, 2003). On the other hand, Si has been shown to lower the point of zero charge (PZC) of Fe minerals (Kingston et al., 1972; Sigg and Stumm, 1981;

Schwertmann and Fechter, 1982; Konhauser et al., 2007a). In this regard, the observed formation of biofilms and EPS (Fig. 5), containing both c-type cytochromes and redox cofactors (Kappler et al., 2021), could represent a strategy to overcome limited bioavailability. This is supported by the high Si setup initially showing the lowest maximum Fe(III) reduction rates and a sharp decrease in the Fe(III) reduction stoichiometry from initially 3.56 ± 0.14 to 2.95 ± 0.27 during the third reductive half cycle, suggesting that a considerable amount of carbon (C) was invested in the synthesis of biomolecules. Consequently, the resulting elevated C/Fe ratio could then have resulted in higher Fe(III) reduction by our *Shewanella* culture via facilitated electron transfer (e.g., Shimizu et al., 2013; Poggenburg et al., 2016, 2018; Cooper et al., 2017), thus explaining the highest maximum Fe(III) reduction rates during the last reductive half cycle.

4.1.3. Microbial Fe cycling – mutual benefit through stimulation of metabolic activity and growth

The co-cultivation of photoferrotrophs and Fe(III)-reducing bacteria, especially in the presence of Si, resulted in a highly dynamic microbial Fe cycle via the mutual stimulation of both activity and growth.

The most obvious mutual benefit is the use of the respective metabolic products of the cycling partner. The metabolic activity of the photoferrotroph resulted in the formation of Fe(III) minerals (and polymeric and complicated organic carbon, C_{org}, consisting of cells, EPS, and their lysate), which, in turn, was used by the Fe(III)-reducers. Conversely, the metabolic activity of Fe(III)-reducing bacteria resulted in the release of Fe(II) and organic products such as acetate (through oxidation of the added lactate), which were used by the photoferrotrophs. Fe(III)-reducing bacteria are known to be able to metabolize a wide variety of Fe(III) minerals and organic compounds (see e.g. O'Loughlin et al., 2019; Dong et al., 2020 for recent studies). Similar to Fe(III)-reducing bacteria, photoferrotrophs are known for their metabolic flexibility and their growth on organic substrates, such as acetate, lactate and yeast extract as well as the potential for fermentative pathways, has previously been reported (e.g., Ehrenreich and Widdel, 1994; Heising et al., 1999; Straub et al., 1999; Imhoff, 2014; Laufer et al., 2017; Bryce et al., 2019). The potential for fermentative pathways could potentially also explain the observed accumulation of formate during the reducing half cycles (Fig. 2). Furthermore, there is strong precedence for the use of co-substrates by photoferrotrophs, which resulted in increased cell numbers (e.g., Heising et al., 1999; Melton et al., 2014). Collectively, these studies support the possibility of a highly dynamic and active microbial Fe cycle formed by photoferrotrophs and Fe(III)-reducing bacteria.

However, the benefits of this microbial Fe cycle may stretch beyond a mutual supply of growth substrates (Cooper et al., 2020). While the use of co-substrates might certainly be beneficial to the individual metabolism by stimulating growth, the constant consumption of the metabolic products by the Fe cycling partner would also have prevented product inhibition, thus allowing the maintenance of enzymatic activity. Furthermore, the excretion of metabolites by photoferrotrophs and Fe(III)-reducing bacteria might also have triggered a mutualistic metabolic response, thus stimulating the growth and activity of each partner (Cooper et al., 2020). This was especially evident when microbial Fe cycling took place in the presence of high concentrations of Si. Both maximum Fe(II) oxidation and Fe(III) reduction rates increased significantly over three microbial Fe cycles. In this regard the poor accessibility of Si-containing ferrihydrite during the first reductive half cycle might have prompted a combined metabolic response by photoferrotrophs and Fe(III)-reducers, thus accelerating microbial Fe cycling.

An additional factor which might have influenced the dynamics of the microbial Fe cycling is the frequency of Fe cycling and the resulting constant supply of substrates. Interestingly, the dynamicity of the Fe cycling might have been self-reinforcing. Especially in the high Si setup we observed that, over time the length of the half cycles became shorter and the maximum rates with which Fe was metabolized increased (Figs. 2 and 3). Barcellos et al. (2018) suggested that higher maximum Fe(III) reduction rates in high periodicity Fe cycles might be related to microbes maintaining their activity due to frequent pulses of reactive substrate. Furthermore, the frequent cycling of the Fe minerals would also have prevented sustained crystal growth. Our combined mineralogical and SEM analyses suggest that even when goethite was formed under low Si conditions, its particle growth was constrained and it likely was of low crystallinity. The overall low crystallinity of goethite and the dominance of SRO Fe(III) (oxyhydr)oxides in the presence of Si likely resulted in increased bioavailability, therefore sustaining highly dynamic microbial Fe cycling.

4.2. Changes in composition of cell-mineral aggregates during microbial Fe cycling

During our experiments, we found the dynamics of polymeric and complicated microbially formed C_{org} and Si to be tightly coupled to Fe(III) mineral precipitation and dissolution. Microbial biomass and Si were sorbed to and co-precipitated with Fe(III) (oxyhydr)oxides during Fe(II) oxidation and released from Fe minerals during Fe(III) mineral reduction (compare Figs. 2, 5 and 6).

Our results correlate well with previous experimental results showing the association of microbial cells and EPS with Fe(III) (oxyhydr)oxides during the activity of photoferrotrophs (cell-Fe(III) mineral aggregates; compare e.g., Posth et al., 2010; Wu et al., 2014; Hao et al., 2016; Martinez et al., 2016; Laufer et al., 2017). The release of polymeric and complicated C_{org} during microbial Fe(III) reduction can either be explained by a decrease in available mineral surface area or the breaking of bonds between the mineral surface and organics. Previous studies reported an increase in dissolved organic carbon of between approximately 13% (Pan et al., 2016) and close to 55% (Adhikari et al., 2017) upon microbial reduction of co-precipitates consisting of ferrihydrite and different organic compounds depending on the C/Fe ratio. Similar to polymeric and complicated microbially formed C_{org}, Si has a high affinity

for Fe(III) (oxyhydr)oxides (e.g., Sigg and Stumm, 1981; Swedlund and Webster, 1999; Phoenix et al., 2003), thus explaining the decreasing concentrations during Fe(II) oxidation. Conversely, the release of Si back into solution during microbial Fe(III) reduction can be explained by the decrease in available reactive surface sites, leading to the destruction of surface complexes between Fe(III) minerals and monosilicic acid (e.g., Pokrovski et al., 2003; Cismasu et al., 2014; Wang et al., 2018).

The overall trend for Si removal showed considerable differences between the high Si and low Si setups. Over three consecutive microbial Fe cycles 52.2 ± 4.4% dissolved Si was removed from solution in the high Si setup, while only 14.0 ± 2.2% of the dissolved Si was removed in the low Si setup. The higher extent of Si removal in the high Si setup might be due to the polymerization of Si at higher concentrations, especially if Fe(III) (oxyhydr)oxides acted as catalysts (Swedlund and Webster, 1999; Swedlund et al., 2010). Once a critical surface saturation is achieved, first oligomers and later polymers are formed (Iler, 1979; Crerar et al., 1981; Hiemstra, 2018; Wang et al., 2018) leading to Si removal (Phoenix et al., 2003). Compared to the low Si setup, where the Si was likely present in monomeric form, this polymerization could also have prevented the competitive replacement of Si by other competing ions, such as polymeric and complicated C_{org} in our case (see e.g. Christl et al., 2012; Hiemstra, 2018), thus preventing its remobilization. Additionally, there is precedence for Si sorption to bacterial cells, which is especially pronounced in the presence of EPS (Lalonde et al., 2005). Since we observed the formation of EPS in our high Si setup, this could be an additional pathway for removing dissolved Si from solution.

Our Si results in combination with fluorescent and electron microscopy further suggest that there might be competition between polymeric and complicated C_{org} (e.g., microbial cells, EPS) and Si for reactive surface sites on the Fe(III) minerals. We observed distinct differences in the Fe(III) (oxyhydr)oxide-Si-C_{org} association depending on the initial Si concentration, where the low Si setup showed the highest and the high Si setup the lowest extent of cell-mineral association. This is in line with previous experimental results which showed a decreased extent of cell-Fe(III) mineral association in the presence of elevated concentrations of Si (e.g., Schad et al., 2019; Thompson et al., 2019). These trends are further in line with a study by Davis et al. (2001), which showed that the exposure of ferrihydrite to increasing concentrations of Si resulted in decreasing amounts of fulvic acid (as a proxy for environmental organic contaminants) being adsorbed onto ferrihydrite thereafter. A potential explanation for the competition between polymeric and complicated C_{org} and Si for Fe(III) mineral reactive surface sites is provided by Dyer et al. (2012). They proposed that at higher Si concentrations, the sorption of Si onto Fe(III) mineral particles takes place earlier during Fe(III) mineral particle formation than at lower Si concentrations. Consequently, in the high Si setup the Si would have directly been adsorbed to the freshly formed Fe(III) minerals, thus forming a Si surface layer (Dyer et al., 2010, 2012), which prevented the adsorption of polymeric and complicated C_{org}.

An exemption hereto is the difference in the extent of C_{org}-Fe mineral association between the no Si and low Si setup, where the former showed a similar or only slightly lower extent of C_{org}-Fe(III) mineral association compared to the latter. Based on the PZC-lowering effect of Si (Kingston et al., 1972; Sigg and Stumm, 1981; Schwertmann and Fechter, 1982; Konhauser et al., 2007a), we would have expected a higher cell-Fe mineral association in the no Si setup than in the low Si setup. However, Cismasu et al. (2014) found that increasing incorporation of Si into ferrihydrite resulted in a decreasing particle size. Additionally, Si has been shown to retard or inhibit the formation of crystalline Fe minerals such as goethite (e.g., Schwertmann et al., 2004; Jones et al., 2009), which has a much lower specific surface area (SSA) than ferrihydrite (Cornell and Schwertmann, 2003). Both are partially reflected in our experimental results, where, when compared to the low Si setup, the Si-free setup showed cell-Fe(III) mineral aggregates which were approximately twice the initial size (compare Sections 3.2 and 3.3) and a prevalence of goethite over ferrihydrite. Therefore, the higher SSA in the low Si setup compared to the no Si setup could have compensated for the Si-induced lower PZC, resulting in comparable (or slightly increased) cell-Fe mineral association in the low Si setup.

However, there is a potential caveat when projecting our experimental results and underlying mechanisms onto an early ocean. Namely, the elevated concentration of Fe(II) (~4–5 mM) we needed to use due to experimental restrictions. Although these concentrations are in line with more recent estimates (e.g. Jiang and Tosca, 2019), which suggested millimolar concentrations of dissolved Fe^{2+} in the early ocean, this view is different to the traditionally assumed low concentrations of Fe(II) (0.03–0.5 mM; Holland, 1973; Morris, 1993). Consequently, the Fe/Si ratio which is between approximately 3 and 6 in our experiments (see Table 1) could have been much lower, approaching Fe/Si ratios between approximately 0.01 and 1 for Si concentrations between 0.5 and 2.2 mM (Siever, 1992; Maliva et al., 2005; Zheng et al., 2016). This could potentially have profoundly influenced the association between cells and Fe minerals. Already at the Fe/Si ratio of ~3 in our high Si setup we observed a much lower extent of cell-Fe mineral association compared to the low Si setup (Fe/Si ratio ~6). Furthermore, Thompson et al. (2019) observed a complete separation between biomass and Fe(III) minerals for the photoferrotroph *Chlorobium phaeoferrooxidans* strain KB01 at a Fe/Si ratio of 0.17. Therefore, if Fe/Si ratios were much lower than in our experiments and potentially even lower than in the Thompson et al. (2019) study, it is sensible to assume that we would have had a complete separation of polymeric and complicated C_{org} and Fe(III) minerals even in the presence of low concentrations of Si (0.5–0.67 mM).

4.3. Changes in mineralogy during microbial Fe cycling under simulated Precambrian ocean conditions

4.3.1. Putative primary seawater precipitate

Based on our combined wet geochemical, mineralogical and microscopic results, the primary seawater precipitates formed through the activity of photoferrotrophs likely con-

sisted of aggregates made up by polymeric and complicated C_{org} (e.g., microbial cells, EPS), Fe(III) (oxyhydr)oxides and Si (Figure 7). Depending on the Si concentration, the polymeric and complicated C_{org} and Si content would have varied, with higher C_{org} and lower Si at low Si concentrations and lower C_{org} and higher Si at high Si concentrations (see Section 4.2). While at high Si concentrations SRO Fe(III) minerals such as ferrihydrite prevailed, we observed the formation of some goethite in addition to SRO Fe(III) minerals at lower Si concentrations. Similar to polymeric and complicated C_{org}, Si has been shown to retard or even inhibit the re-crystallization of poorly crystalline Fe(III) minerals into crystalline Fe(III) minerals such as goethite (e.g. Schwertmann et al., 2004; Jones et al., 2009; ThomasArrigo et al., 2017; Zhou et al., 2018). Therefore, depending on the exact Si concentrations in the early ocean, the primary C_{org}-Fe(III) mineral-Si aggregates could have contained some goethite in addition to SRO Fe(III) minerals such as ferrihydrite.

However, not only the Si concentration could have influenced the composition of the primary C_{org}-Fe(III) mineral-Si aggregates, but also the dissolved Fe^{2+} concentration. While our experimental conditions are in line with results of Jiang and Tosca (2019), who suggested millimolar dissolved Fe^{2+} concentrations for the early ocean, traditionally an order of magnitude lower Fe^{2+} concentrations have been suggested (see Section 4.2). This would have resulted in much lower Fe/Si ratios, thus likely not only preventing the co-deposition of polymeric and complicated C_{org} and Fe(III) minerals but also preventing the formation of crystalline Fe(III) minerals like goethite. Consequently, depending on the exact combination of Fe^{2+} and Si concentrations the primary seawater precipitate could have been a C_{org}-Fe(III) mineral-Si composite (e.g., Konhauser et al., 2007a; Fischer and Knoll, 2009; Alibert, 2016) or possibly even a Fe(III) mineral-Si gel as advocated by some other studies (e.g., Wu et al., 2012; Reddy et al., 2016; Zheng et al., 2016).

4.3.2. Mineralogical products of microbial Fe(III) reduction - Secondary seawater precipitates

Goethite was identified as major secondary Fe(III) mineral phase in our no and low Si setups following microbial Fe(III) reduction and a SRO Fe(III) mineral phase in our high Si setup. However, we found no indication for the formation of typical Fe(II)-bearing minerals like magnetite or siderite in our experiments and the identity of the secondary Fe(II) mineral phases in our experiments remained ambiguous.

The formation of goethite following microbial Fe(III) reduction in our experiments is reasonable given the possible re-crystallization of a poorly crystalline precursor mineral phase following the adsorption of low concentrations of Fe(II) ($\sim$0.1 mmol g^{-1} ferrihydrite; Hansel et al., 2005). Additionally, it has been shown that Fe(III)-reducing microbes preferentially utilize poorly crystalline Fe(III) minerals over crystalline minerals such as goethite (e.g., Roden and Zachara, 1996; Roden, 2003; Bonneville et al., 2004, 2009). Consequently, the goethite which was formed during microbial Fe(II) oxidation in our experiments would be preserved following microbial Fe(III) reduction.

The observed absence of magnetite in our experiments is in line with other experimental results by Zachara et al. (2002) and O'Loughlin et al. (2010) who found that at high rates of microbial Fe(III) reduction or in the presence of natural organic matter or competing oxyanions such as Si, no magnetite was formed. Instead, they found the formation of either siderite or green rust. Both, polymeric and complicated C_{org} and Si are well known for retarding or inhibiting Fe(II)-induced secondary mineral transformation either through blocking reactive surface sites or by complexing Fe(II) (e.g. Schwertmann et al., 2004; Jones et al., 2009; ThomasArrigo et al., 2017; Zhou et al., 2018). Surprisingly, however, we also found no indication of siderite precipitation, although our geochemical conditions should have favored its formation. One potential explanation might be the complexation of Fe(II) by organic matter (ThomasArrigo et al., 2017), which is indicated by generally high dissolved Fe^{2+} concentrations (>80%) in our experiments. Furthermore, recent studies suggest that siderite growth kinetics are slow even under highly oversaturated conditions (Jiang and Tosca, 2019; Jiang and Tosca, 2020) and instead Fe(II)-silicate precipitation controlled aqueous Fe(II) concentrations (Jiang and Tosca, 2019).

However, the precipitation of Fe(II)-silicates requires pH values > 7.5 (e.g., Tosca et al., 2016; Rasmussen et al., 2020), which is higher than the pH of 7.1 in our experiments. Although we did not follow changes in pH during our experiments, it is possible that the pH increased to the required values during microbial Fe(III) reduction (see Section 3.1, Eq. (1)). Furthermore, experimental studies by Konhauser et al. (2007b) and Percak-Dennett et al. (2011), with experimental conditions similar to ours, observed the formation of Fe(II)-silicates, thus supporting their possible formation in our experiments. In fact, the observations of Percak-Dennett et al. (2011) are well in line with our findings. Upon microbial reduction of a Fe(III)-Si gel they found neither the formation siderite despite an up to 1000-fold oversaturation nor the formation of magnetite. In their study the primary mineral phase did not undergo any significant transformation (re-crystallization), although they suggest the possible presence of a "primitive smectite-like phase", where some of the Fe(II) was re-adsorbed to the Fe(III)-Si-gel.

More recent results by Hinz et al. (2021) suggest that the presence of small quantities of Fe(III) can induce the precipitation of Fe(II)-bearing silicates even at pH 6.5 or 7.0, possibly resulting in the formation of secondary Fe minerals such as a low-Fe(III) greenalite (Johnson et al., 2018). Even though our mineralogical data regarding the identity of the secondary Fe(II)-bearing minerals are ambiguous, based on previous studies by Percak-Dennett et al. (2011), Johnson et al. (2018) and Hinz et al. (2021) it appears possible that the microbial reduction of our primary C_{org}-Fe(III) mineral-Si composite resulted in the formation of a secondary Fe(II)-, possibly mixed Fe(II)/Fe(III)-, silicate, which would also explain some of the greenalite previously reported in BIFs (see Section 4.4.2). This is further supported by our findings, where, depending on the Si concen-

tration, we found a removal of dissolved Si from solution of between approx. 14% and 52% over the course of our experiments, possibly due to the formation of an X-ray amorphous secondary Fe(II)-Si mineral (or Fe(II)-Fe(III)-Si mineral) phase (Fig. 7). These results likely also apply to Fe/Si ratios much lower than in our experimental study (see Section 4.2), consequently resulting in the effective inhibition of siderite and magnetite formation.

4.4. The relevance of microbial water column Fe cycling for the deposition of BIFs

4.4.1. Factors controlling microbial Fe cycling during BIF deposition

The extent to which microbial Fe cycling in an ancient ocean water column would have influenced the secondary mineral (trans)formation during the deposition of BIFs is determined by three major factors: (1) depth of the photic zone, (2) particle size and resulting sedimentation rate, and (3) the maximum Fe(II) oxidation and Fe(III) reduction rates. These factors would have determined the residence time of mineral particles within the photic zone and how many Fe cycles these particles could have undergone before leaving the photic zone.

The maximum depth of the photic zone over the shelf is influenced by the particle loading in the water column (bacteria, minerals, organics, etc.), which can vary due to volcanic eruptions, bacterial plumes or, closer to the shore, increased detrital sediment input. In modern oceans, 95% of the light is absorbed within the first approximately 100 m of the water column. In turbid coastal waters, this depth may be reduced to a few meters (Stewart, 2008; Hempel et al., 2016). In the Black Sea, anoxygenic phototrophs have been reported to occur in depths between 60 and 120 m (Repeta et al., 1989; Manske et al., 2005). Crowe et al. (2008) reported the presence of putative photoferrotrophs from depths between 110 and 120 m in Lake Matano (Indonesia), a modern-day analogue for ferruginous Archean oceans. In contrast, Llirós et al. (2015) reported > 90% of the photosynthetically active light to have been absorbed within the first 10 m of the ferruginous water column of Kabuno Bay, Lake Kivu, Eastern Africa (DR Kongo), with peak *bacteriochlorophyll e* concentrations between 10 and 12 m water depth. In order to address these contrasting conditions, we will consider two endmember scenarios where (1) photoferrotrophy occurs until depths of 100 m before mineral particles exit the photic zone and (2) photoferrotrophs are only active within the top 10 m of the water column.

Considering these two endmember scenarios, microbial Fe cycling linking photoferrotrophy and microbial Fe(III) reduction could have taken place during 5% (10 m photic depth) to 50% (100 m photic depth) of the time required by cell-Fe(III) mineral aggregates to be deposited seafloor (depth of the shelf, ≤200 m; Table 2, supplementary text S9). However, these calculations would also need to consider the maximum Fe(II) oxidation rates, which are dependent on the concentrations of Fe(II). Unfortunately, due to experimental constraints to obtain a sufficient quantity of Fe minerals for analysis, our experiments required mM concentrations of Fe(II). While this is in line with estimations for the upper end of concentrations assumed for the Precambrian ocean (several mM; Jiang and Tosca, 2019), our concentrations exceeded estimates at the lower end of the assumed concentrations by approximately an order of magnitude (0.03–0.5 mM; Holland, 1973; Morris, 1993). Therefore, in order to also consider these low concentrations and instead of trying to adapt our experimentally derived maximum rates to them, we compare the time required for three microbial Fe cycles in our experiments to the time theoretically required by the mineral particles to sink through the photic zone. Despite the discrepancy in the Fe(II) concentrations, this should thus still provide us with an estimate about the extent of microbial Fe cycling (the number of cycles) in the water column during the deposition of BIFs.

The results of our estimates regarding the extent of microbial Fe cycling occurring at different Si concentrations are summarized in Table 2. Due to the similarity in the results of the low Si and high Si setups, and in order to consider the most conservative scenario, we will focus on the high Si setup in the following discussion. If the photic zone was relatively shallow (10 m), then microbial water column Fe cycling likely only played a minor role. The average photic zone residence time of cell-mineral aggregates would have been 11.07 days, whereas the majority of the aggregates would have passed through the photic zone in only 1.94 days, allowing for less than one microbial Fe cycle (Table 2, supplementary text S9). If, on the other hand, the photic zone extended to approximately 100 m, the influence of microbial Fe cycling would have been much more prominent. The average photic zone residence time of any given aggregate would have increased to ca. 110 days, with the majority of aggregates exiting the photic zone after ca. 19 days. Consequently, individual aggregates might, on average, have been cycled more than 8 times (8.74 times), with the majority having been cycled at least 1.53 times before leaving the photic zone. Our values bracket and are in good agreement with results of Bauer et al. (2020), who estimated that Fe(II) in the Malili lake system (as modern-day analogue to the Precambrian ocean) is cycled 2–3 times before being removed from the system through sedimentation and burial. Similar to our study, Roland et al. (2021) observed that in Kabuno Bay (as another modern-day analogue), the Fe was cycled up to 11 times before sedimentation.

Another consequence of the attenuation of light with increasing water depth is that this influences the relative importance of photoferrotrophy vs. microbial Fe(III) reduction. In our experiments, the oxidative half cycles were performed at or close to light saturation, which generally resulted in net Fe(II) oxidation during oxidative half cycles (despite Fe(III) reduction probably occurring at the same time). However, considering decreasing light availability at increasing water depth, the efficacy with which Fe(II) is oxidized photosynthetically will also be reduced. Indeed, Kappler et al. (2005) suggested that at 100 m depth the rate with which Fe(II) is oxidized would be only 20% of the surface level. In contrast, Fe(III)-reducing bacteria would be unaffected by changing light levels. Therefore,

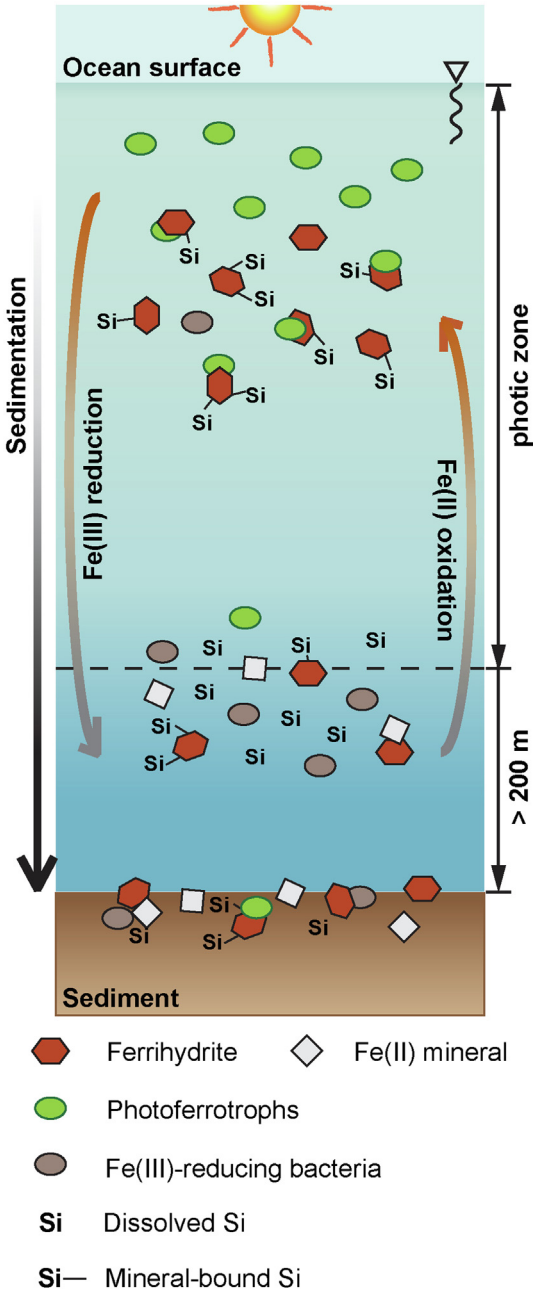

Fig. 7. Microbial Fe cycling occurring in the water column during the deposition of BIFs. Hydrothermally derived Fe^{2+} is oxidized by photoferrotrophs, resulting in the co-precipitation of ferrihydrite (Fh), polymeric and complicated C_{org} (microbial cells, EPS) and Si. These cell-Fe(III) mineral aggregates are then reduced by Fe(III)-reducing bacteria within the water column, resulting in the reduction of Fh, the formation of a Fe(II) mineral (siderite and/or a Fe(II)-silicate) and the concomitant release of Si and C_{org} from the aggregates. The co-occurrence of photoferrotrophs and Fe(III)-reducing bacteria results in a highly dynamic microbial Fe cycling. With waning light intensity deeper in the water column the Fe cycling is increasingly dominated by microbial Fe(III) reduction and ceases once individual cell-mineral aggregates sink below the photic depth, resulting in the deposition of ferrihydrite and a Fe(II) mineral mixture at the ocean floor together with polymeric and complicated C_{org} and Si, albeit the latter two are to some extent released from the aggregates during water column Fe cycling.

depending on the water depth, the extent to which Fe is cycled within and below the photic zone would be affected.

An additional factor expected to influence Fe cycling is the use of co-substrates by photoferrotrophs, i.e., the simultaneous use of Fe(II) and fatty acids (see Section 3.1). Past studies showed that the presence of both Fe(II) and fatty acids increased cell numbers (Heising et al., 1999; Melton et al., 2014). This either resulted in enhanced Fe(II) oxidation, or, depending on the substrate preference, fatty acids were consumed before Fe(II), thus delaying Fe(II) oxidation (Melton et al., 2014). Similarly, Croal et al. (2009) found that the presence of a co-substrate (H_2) limited Fe(II) oxidation by their tested photoferrotrophic strains. Additionally, high frequency redox oscillations have been found to increase the rate with which Fe(III)-reducing bacteria reduce Fe(III) (e.g., Ginn et al., 2017; Barcellos et al., 2018). This has been attributed to the ability of bacteria to maintain their activity during shorter redox oscillations and to their constant stimulation by repeated pulses of substrate. In turn, the constant re-supply of Fe(II) would have a similar stimulating effect on photoferrotrophs, thus enhancing the efficacy with which they re-oxidize the Fe(II), resulting in a highly efficient microbial Fe cycle even at reduced light conditions deeper in the photic zone (Fig. 7).

4.4.2. Consequences of microbial Fe cycling for the mineralogy and composition of primary BIF sediments

The composition of the primary BIF sediment would have been heavily dependent on the frequency of microbial Fe cycling during the initial deposition of BIFs and the seawater Si concentration. At high seawater Si concentrations (approaching saturation with regards to amorphous Si) and moderate water column Fe cycling (1 full cycle) during the deposition of BIF, the composition of the primary sediment would have been dominated by a primary SRO Fe(III) (oxyhydr)oxide (e.g., ferrihydrite) with up to 10% of a Fe(II) mineral. In contrast, if there would have been extensive Fe cycling (over 8 full cycles), the primary sediment would have consisted of up to 50% SRO Fe(III) (oxyhydr)oxide and 50% of a Fe(II) mineral phase (Fig. 7).

At low seawater Si concentrations (saturation with regards to cristobalite, 0.67 mM; Maliva et al., 2005) the Fe(III) mineral phase would have consisted of a mixture of a SRO Fe(III) mineral (ferrihydrite) and goethite. Additionally, compared to high seawater Si concentrations the formation of an Fe(II) mineral phase would have been limited. In case of moderate water column Fe cycling (1 full cycle), no Fe(II) mineral phase would have been formed and even during extensive Fe cycling (over 8 full cycles) the extent of Fe(II) mineral formation would not have exceeded 10%. However, both at low and high seawater Si concentrations, the reductive dissolution of the Fe(III) mineral phase during microbial Fe(III) reduction would have resulted in the release of polymeric and complicated C_{org} and Si from the cell-mineral aggregates (Fig. 7).

Our experimental data suggest the possible formation of an (X-ray amorphous) Fe(II)-Si mineral phase instead of siderite or magnetite during microbial water column Fe cycling. Previous studies have advanced the idea that an

Table 2
Summary of sedimentation rates, water column residence time and parameters determining microbial Fe cycling inside the photic zone for Si concentrations bracketing expected Precambrian ocean concentrations (0.67–2.2 mM Si).

	Low Si	High Si
Time metabolically active [d] [a]	40	38
Aggregate size [μm]	12.95 (17.90 ± 16.40)	13.23 (16.01 ± 12.72)
Corrected sedimentation rate [m h^{-1}]	0.25 (0.87 ± 1.65)	0.22 (0.51 ± 1.05)
Aggregate water column residence time [d] [b]	33.59 (280 ± 782.69)	38.75 (221.44 ± 1126.54)
10 m photic zone		
Time inside photic zone [d]	1.68 (14.05 ± 39.13)	1.94 (11.07 ± 56.33)
Number of Fe cycles [c]	0.13 (1.05 ± 2.94)	0.15 (0.87 ± 4.45)
100 m photic zone		
Time inside photic zone [d]	16.79 (140.45 ± 391.35)	19.37 (110.72 ± 563.27)
Number of Fe cycles [c]	1.26 (10.53 ± 29.35)	1.53 (8.74 ± 44.47)

Calculated values are based on results for particle size and sedimentation rate (see Section 3.3 and supplementary text S1). All values represent median values. Values in parentheses are mean ± standard deviation. n = 148 for "low Si" and n = 135 for "high Si". A full breakdown of all calculations is provided in supplementary text S9 and a complete distribution of settling velocities given in Fig. S8. All calculations are based number-averaged rather than mass-averaged aggregate sizes (see Section 3.3).

[a] Based on 3 microbial Fe cycles performed in our experiments. We define the time until either ≥ 95% of the Fe(II) was oxidized or ≥ 70% of the initially oxidized Fe(II) was reduced again as "metabolically active."

[b] Assuming BIFs were deposited at the depth of the shelf, at depths exceeding modern storm-wave base.

[c] Based on 3 microbial Fe cycles performed in our experiments.

Fe(II)-silicate, such as greenalite, instead of Fe(III) (oxyhydr)oxides could have been the primary seawater precipitate during BIF deposition thus forming the precursor sediment to BIFs (e.g., Rasmussen et al., 2017, 2021; Muhling and Rasmussen, 2020). This view has been contested based on the slightly alkaline pH required for its formation (7.5–8.0 or higher; e.g. Klein, 2005; Beukes and Gutzmer, 2008; Tosca et al., 2016; Halevy et al., 2017; Rasmussen et al., 2020), which has been suggested to be at odds with the slightly acidic to circumneutral pH conditions of an Archean to early Paleoproterozoic ocean (Halevy and Bachan, 2017; Krissansen-Totton et al., 2018) and the low probability of basin-scale secondary oxidation (Robbins et al., 2019). Based on our mineralogical data a layered Fe(II) mineral or an amorphous Fe(II)-silicate (potentially a precursor to a mineral such as greenalite) could have been formed during microbial water column Fe cycling from a primary Fe(III) (oxyhydr)oxide such as ferrihydrite or goethite. In this regard the Fe(II) mineral phase would represent a "secondary seawater precipitate", which would explain its apparent primary features deduced from petrographic studies (e.g., Rasmussen et al., 2013; Rasmussen et al., 2015; Rasmussen et al., 2017). Consequently, depending on the seawater Si concentration and the extent of microbial water column Fe cycling, the minerals ultimately deposited on the seafloor would have been a Fe(III) (oxyhydr)oxide (ferrihydrite or goethite) mixed with 10–50% of a Fe(II) mineral phase such as a Fe(II)-silicate.

In contrast to Fe(III) (oxyhydr)oxides and Fe(II)-silicates, siderite and magnetite likely formed later during sedimentary diagenesis as suggested by various petrographic and isotope geochemical studies (e.g. Beukes, 1973; Johnson et al., 2003, 2008, 2013; Fischer et al., 2009; Pecoits et al., 2009; Heimann et al., 2010; Steinhoefel et al., 2010; Craddock and Dauphas, 2011; Wang et al., 2015; Teixeira et al., 2017). In the open water column, siderite precipitation was likely limited by low growth kinetics (Jiang and Tosca, 2020), while polymeric and complicated C_{org} and Si that were co-precipitated with the Fe(III) (oxyhydr)oxides inhibited magnetite formation. Depending on the relative abundance of Fe(II), HCO_3^- and Fe(III) (oxyhydr)oxides, siderite might have been formed under semi-secluded conditions in the soft sediment if Fe(II) and HCO_3^- accumulated to concentrations above a critical threshold (Heimann et al., 2010; Jiang and Tosca, 2020). Alternatively, siderite could have been formed during low-grade metamorphism through the thermochemical reduction of primary Fe(III) (oxyhydr)oxides coupled to organic carbon oxidation (Köhler et al., 2013; Posth et al., 2013; Halama et al., 2016).

Magnetite has been found to structurally overgrow hematite and siderite (e.g. Ayres, 1972; Ewers and Morris, 1981; Beukes and Gutzmer, 2008; Pecoits et al., 2009; Rasmussen and Muhling, 2018), thus rather supporting its formation later in the paragenetic sequence during sediment diagenesis or possibly low-grade metamorphism. Magnetite formation could have been enabled by the release of polymeric and complicated C_{org} and Si during Fe cycling in the water column (Fig. 7). The lower extent of adsorbed Si and polymeric and complicated C_{org} could have facilitated the adsorption of Fe(II) required for the solid-state conversion of the remaining ferrihydrite into magnetite (Hansel et al., 2005). Additionally, the progressive burial of the sediment could have reduced or cut off the infiltration of seawater into the sediment, and therefore, also the supply of seawater-derived HCO_3^-, thus favoring the formation of magnetite over siderite (Heimann et al., 2010).

5. CONCLUSIONS

Past experimental studies evaluating the mechanisms underlying the (trans-)formation of BIFs often considered only a single mechanism concerning either; (1) the initial

mineral deposition, driven either biotically by photoferrotrophs or cyanobacteria or abiotically through precipitation of Fe(II)-silicates, or (2) post-depositional alteration during (microbial) diagenesis or low-grade metamorphism. Here we experimentally determined how, and to which extent, two such mechanisms suggested to have played a major role in the genesis of BIFs, water column photoferrotrophy and microbial Fe(III) reduction, may have interacted during the genesis of BIFs. To this end, we co-cultivated a marine photoferrotroph and a marine Fe(III)-reducing culture under conditions relevant for the Precambrian ocean. We specifically determined; (1) how Fe(II)-oxidizing and Fe(III)-reducing bacteria would have interacted during repeated and dynamic microbial water column Fe cycling, and (2) how this would have influenced the nature, composition and mineralogy of primary BIF sediments.

Our results demonstrate that the co-cultivation of photoferrotrophs and Fe(III)-reducing bacteria resulted in highly dynamic microbial Fe cycling, which persisted over several consecutive Fe cycles. Generally, Fe(II) oxidation resulted in the co-precipitation of microbially derived organics, Fe(III) minerals (ferrihydrite and/or goethite) and Si, whereas Fe(III) reduction resulted in the reductive dissolution of Fe(III) minerals, the release of organics and Si, and, depending on the Si concentration, the formation of varying amounts of a Fe(II) mineral phase (possibly a Fe(II)-bearing silicate). While some of the Fe(II)-silicates in BIF might therefore be considered as having formed during microbial Fe cycling in the water column, we found no clear indication for siderite and no evidence for magnetite formation in any of our experiments. Furthermore, although our study suggests that Fe(III) minerals instead of the Fe(II)-bearing silicates would have been the primary seawater precipitate, we stress that water column Fe cycling might potentially have facilitated the formation of some Fe(II)-bearing silicates and their subsequent deposition on the seafloor. In short, we suggest that while ferrihydrite as well as a Fe(II)-bearing silicate likely formed during microbial Fe cycling in the water column, siderite and magnetite formed during BIF sediment diagenesis.

DECLARATION OF COMPETING INTEREST

The authors declare that they have no known competing financial interests or personal relationships that could have appeared to influence the work reported in this paper.

ACKNOWLEDGEMENTS

The authors would like to thank Dr. Y. Bai and K. Wunsch for their experimental support. Dr. Y. Bai is further thanked for her comments which helped to improve this manuscript. Dr. H. Schulz and T. Bayer are acknowledged for advice and support with SEM analysis. The authors would further like to thank Dr. C. Bryce and L. Grimm for their help with flow cytometry. E. Röhm is acknowledged for her help with HPLC measurements. Dr. M. Muehe, Dr. C. Bryce, Dr. M. Maisch, Dr. M. Patzner and J. Sorwat are further acknowledged for fruitful discussions on experimental design and data interpretation. We would also like to thank two anonymous reviewers whose comments helped improving this manuscript. The authors further acknowledge infrastructural support by the Deutsche Forschungsgemeinschaft (DFG, German Research Foundation) under Germany's Excellence Strategy, cluster of Excellence EXC2124, project ID 390838134. This study was supported by grants from the German Research Foundation (DFG) to AK and a Natural Sciences and Engineering Research Council (NSERC) grant to KOK (RGPIN-2020-05189). JMB is supported by a UKRI Future Leaders Fellowship, MR/V023918/1.

APPENDIX A. SUPPLEMENTARY MATERIAL

Supplementary material to this article can be found online at https://doi.org/10.1016/j.gca.2022.05.016.

REFERENCES

Adhikari D., Zhao Q., Das K., Mejia J., Huang R., Wang X., Poulson S. R., Tang Y., Roden E. E. and Yang Y. (2017) Dynamics of ferrihydrite-bound organic carbon during microbial Fe reduction. *Geochim. Cosmochim. Acta* **212**, 221–233.

Alibert C. (2016) Rare earth elements in Hamersley BIF minerals. *Geochim. Cosmochim. Acta* **184**, 311–328.

Amthauer G. and Rossman G. R. (1984) Mixed Valence of iron in mienrals with cation clusters. *Phys. Chem. Miner.* **11**, 37–51.

Ayres D. (1972) Genesis of iron-bearing minerals in banded iron formation mesobands in the Dales Gorge Member, Hamersley Group, Western Australia. *Econ. Geol.* **67**, 1214–1233.

Barcellos D., Cyle K. T. and Thompson A. (2018) Faster redox fluctuations can lead to higher iron reduction rates in humid forest soils. *Biogeochemistry* **137**, 367–378.

Bauer K. W., Byrne J. M., Kenward P., Simister R. L., Michiels C. C., Friese A., Vuillemin A., Henny C., Nomosatryo S., Kallmeyer J., Kappler A., Smit M. A., Francois R. and Crowe S. A. (2020) Magnetite biomineralization in ferruginous waters and early Earth evolution. *Earth Planet. Sci. Lett.* **549**, 116495.

Bekker A., Planavsky N., Rasmussen B., Krapez B., Hofmann A., Slack J., Rouxel O. and Konhauser K. O. (2014) *Iron formations: their origins and implications for ancient seawater chemistry*, second ed. Elsevier, Netherlands, pp. 561–628.

Bekker A., Slack J. F., Planavsky N., Krapež B., Hofmann A., Konhauser K. O. and Rouxel O. J. (2010) Iron formation: the sedimentary product of a complex interplay among mantle, tectonic, oceanic, and biospheric processes. *Econ. Geol.* **105**, 467–508.

Bergerhoff G., Brown I. D. and Allen F. (1987) Crystallographic databases. *International Union of Crystallography, Chester* **360**, 77–95.

Beukes N. J. (1973) Precambrian iron-formations of southern Africa. *Econ. Geol.* **68**, 960–1004.

Beukes N. J. and Gutzmer J. (2008) Origin and paleoenvironmental significance of major iron formations at the Archean-Paleoproterozoic boundary. *Rev. Econ. Geol.* **15**, 5–47.

Blake R., Chang S. and Lepland A. (2010) Phosphate oxygen isotopic evidence for a temperate and biologically active Archaean ocean. *Nature* **464**, 1029–1032.

Bonneville S., Behrends T. and Van Cappellen P. (2009) Solubility and dissimilatory reduction kinetics of iron(III) oxyhydroxides: a linear free energy relationship. *Geochim. Cosmochim. Acta* **73**, 5273–5282.

Bonneville S., Van Cappellen P. and Behrends T. (2004) Microbial reduction of iron(III) oxyhydroxides: effects of mineral solubility and availability. *Chem. Geol.* **212**, 255–268.

Bryce C., Blackwell N., Straub D., Kleindienst S. and Kappler A. (2019) Draft genome sequence of *Chlorobium* sp. strain N1, a

marine Fe(II)-oxidizing green sulfur bacterium. *Microbiol. Resour. Announc.* **8**.

Chen C. and Thompson A. (2018) Ferrous iron oxidation under varying pO_2 levels: the effect of Fe(III)/Al(III) oxide minerals and organic matter. *Environ. Sci. Technol.* **52**, 597–606.

Christl I., Brechbühl Y., Graf M. and Kretzschmar R. (2012) Polymerization of silicate on hematite surfaces and its influence on arsenic sorption. *Environ. Sci. Technol.* **46**, 13235–13243.

Cismasu A. C., Michel F. M., Tcaciuc A. P. and Brown G. E. (2014) Properties of impurity-bearing ferrihydrite III. Effects of Si on the structure of 2-line ferrihydrite. *Geochim. Cosmochim. Acta* **133**, 168–185.

Cismasu A. C., Michel F. M., Tcaciuc A. P., Tyliszczak T. and Brown G. E. (2011) Composition and structural aspects of naturally occurring ferrihydrite. *C. R. Geosci.* **343**, 210–218.

Cloud P. E. (1973) Paleoecological significance of the banded iron-formation. *Econ. Geol.* **68**, 1135–1143.

Cooper R. E., Eusterhues K., Wegner C.-E., Totsche K. U. and Küsel K. (2017) Ferrihydrite-associated organic matter (OM) stimulates reduction by *Shewanella oneidensis* MR-1 and a complex microbial consortia. *Biogeosciences* **14**.

Cooper R. E., Wegner C.-E., Kügler S., Poulin R. X., Ueberschaar N., Wurlitzer J. D., Stettin D., Wichard T., Pohnert G. and Küsel K. (2020) Iron is not everything: unexpected complex metabolic responses between iron-cycling microorganisms. *ISME J.* **14**, 2675–2690.

Cornell R. M. and Schwertmann U. (2003) *The Iron Oxides: Structure, Properties, Reactions, Occurrences and Uses*. Wiley-VCH Verlag, Weinheim, p. 703.

Craddock P. R. and Dauphas N. (2011) Iron and carbon isotope evidence for microbial iron respiration throughout the Archean. *Earth Planet. Sci. Lett.* **303**, 121–132.

Crerar D. A., Axtmann E. V. and Axtmann R. C. (1981) Growth and ripening of silica polymers in aqueous solutions. *Geochim. Cosmochim. Acta* **45**, 1259–1266.

Croal L. R., Jiao Y., Kappler A. and Newman D. K. (2009) Phototrophic Fe(II) oxidation in an atmosphere of H_2: implications for Archean banded iron formations. *Geobiology* **7**, 21–24.

Crowe S. A., Jones C., Katsev S., Magen C., O'Neill A. H., Sturm A., Canfield D. E., Haffner G. D., Mucci A., Sundby B. and Fowle D. A. (2008) Photoferrotrophs thrive in an Archean Ocean analogue. *Proc. Natl. Acad. Sci.* **105**, 15938–15943.

Crowe S. A., Paris G., Katsev S., Jones C., Kim S.-T., Zerkle A. L., Nomosatryo S., Fowle D. A., Adkins J. F., Sessions A. L., Farquhar J. and Canfield D. E. (2014) Sulfate was a trace constituent of Archean seawater. *Science* **346**, 735–739.

Davis C. C., Knocke W. R. and Edwards M. (2001) Implications of aqueous silica sorption to iron hydroxide: mobilization of iron colloids and interference with sorption of arsenate and humic substances. *Environ. Sci. Technol.* **35**, 3158–3162.

De Wit M. J. and Furnes H. (2016) 3.5-Ga hydrothermal fields and diamictites in the Barberton Greenstone Belt – Paleoarchean crust in cold environments. *Sci. Adv.* **2**, e1500368.

Derry L. A. (2015) Causes and consequences of mid-Proterozoic anoxia. *Geophys. Res. Lett.* **42**, 8538–8546.

Dippon U., Schmidt C., Behrens S. and Kappler A. (2015) Secondary mineral formation during ferrihydrite reduction by *Shewanella oneidensis* MR-1 depends on incubation vessel orientation and resulting gradients of cells, Fe^{2+} and Fe minerals. *Geomicrobiol. J.* **32**, 878–889.

Dong Y., Sanford R. A., Boyanov M. I., Flynn T. M., O'Loughlin E. J., Kemner K. M., George S., Fouke K. E., Li S., Huang D., Li S. and Fouke B. W. (2020) Controls on Iron Reduction and Biomineralization over Broad Environmental Conditions as Suggested by the Firmicutes *Orenia metallireducens* Strain Z6. *Environ. Sci. Technol.* **54**, 10128–10140.

Downs R. T. and Hall-Wallace M. (2003) The American Mineralogist crystal structure database. *Am. Mineral.* **88**, 247–250.

Dyer L. G., Fawell P. D., Newman O. and Richmond W. R. (2010) Synthesis and characterisation of ferrihydrite/silica co-precipitates. *J. Colloid Interface Sci.* **348**, 65–70.

Dyer L. G., Chapman K. W., English P., Saunders M. and Richmond W. R. (2012) Insights into the crystal and aggregate structure of Fe^{3+} oxide/silica co-precipitates. *Am. Mineral.* **97**, 63–69.

Ehrenreich A. and Widdel F. (1994) Anaerobic oxidation of ferrous iron by purple bacteria, a new type of phototrophic metabolism. *Appl. Environ. Microbiol.* **60**, 4517–4526.

Eickhoff M., Obst M., Schröder C., Hitchcock A. P., Tyliszczak T., Martinez R. E., Robbins L. J., Konhauser K. O. and Kappler A. (2014) Nickel partitioning in biogenic and abiogenic ferrihydrite: the influence of silica and implications for ancient environments. *Geochim. Cosmochim. Acta* **140**, 65–79.

Eusterhues K., Wagner F. E., Häusler W., Hanzlik M., Knicker H., Totsche K. U., Kögel-Knabner I. and Schwertmann U. (2008) Characterization of ferrihydrite-soil organic matter coprecipitates by X-ray diffraction and Mössbauer spectroscopy. *Environ. Sci. Technol.* **42**, 7891–7897.

Ewers W. E. and Morris R. C. (1981) Studies of the Dales Gorge member of the Brockman iron formation, Western Australia. *Econ. Geol.* **76**, 1929–1953.

Fischer W. W. and Knoll A. H. (2009) An iron shuttle for deepwater silica in late Archean and early Paleoproterozoic iron formation. *Geol. Soc. Am. Bull.* **121**, 222–235.

Fischer W. W., Schroeder S., Lacassie J. P., Beukes N. J., Goldberg T., Strauss H., Horstmann U. E., Schrag D. P. and Knoll A. (2009) Isotopic constraints on the Late Archean carbon cycle from the Transvaal Supergroup along the western margin of the Kaapvaal Craton, South Africa. *Precambrian Res.* **169**, 15–27.

Galili N., Shemesh A., Yam R., Brailovsky I., Sela-Adler M., Schuster E. M., Collom C., Bekker A., Planavsky N., Macdonald F. A., Préat A., Rudmin M., Trela W., Sturesson U., Heikoop J. M., Aurell M., Ramajo M. and Halevy I. (2019) The geologic history of seawater oxygen isotopes from marine iron oxides. *Science* **365**, 469–473.

Gauger T., Byrne J. M., Konhauser K. O., Obst M., Crowe S. A. and Kappler A. (2016) Influence of organics and silica on Fe(II) oxidation rates and cell–mineral aggregate formation by the green-sulfur Fe(II)-oxidizing bacterium *Chlorobium ferrooxidans* KoFox–Implications for Fe(II) oxidation in ancient oceans. *Earth Planet. Sci. Lett.* **443**, 81–89.

Ginn B., Meile C., Wilmoth J., Tang Y. and Thompson A. (2017) Rapid iron reduction rates are stimulated by high-amplitude redox fluctuations in a tropical forest soil. *Environ. Sci. Technol.* **51**, 3250–3259.

Gole M. J. and Klein C. (1981) Banded iron-formations through much of Precambrian time. *J. Geol.* **89**, 169–183.

Gumsley A. P., Chamberlain K. R., Bleeker W., Söderlund U., de Kock M. O., Larsson E. R. and Bekker A. (2017) Timing and tempo of the Great Oxidation Event. *Proc. Natl. Acad. Sci.* **114**, 1811–1816.

Halama M., Swanner E. D., Konhauser K. O. and Kappler A. (2016) Evaluation of siderite and magnetite formation in BIFs by pressure–temperature experiments of Fe(III) minerals and microbial biomass. *Earth Planet. Sci. Lett.* **450**, 243–253.

Halevy I., Alesker M., Schuster E. M., Popovitz-Biro R. and Feldman Y. (2017) A key role for green rust in the Precambrian oceans and the genesis of iron formations. *Nat. Geosci.* **10**, 135–139.

Halevy I. and Bachan A. (2017) The geologic history of seawater pH. *Science* **355**, 1069–1071.

Han X., Tomaszewski E. J., Sorwat J., Pan Y., Kappler A. and Byrne J. M. (2020) Effect of Microbial Biomass and Humic Acids on Abiotic and Biotic Magnetite Formation. *Environ. Sci. Technol.* **54**, 4121–4130.

Hansel C. M., Benner S. G. and Fendorf S. (2005) Competing Fe (II)-induced mineralization pathways of ferrihydrite. *Environ. Sci. Technol.* **39**, 7147–7153.

Hansel C. M., Benner S. G., Neiss J., Dohnalkova A., Kukkadapu R. K. and Fendorf S. (2003) Secondary mineralization pathways induced by dissimilatory iron reduction of ferrihydrite under advective flow. *Geochim. Cosmochim. Acta* **67**, 2977–2992.

Hansen H. C. B. (1989) Composition, stabilization, and light absorption of Fe(II) Fe(III) hydroxyl-carbonte ('green rust'). *Clay Miner.* **24**, 663–669.

Hao L., Guo Y., Byrne J. M., Zeitvogel F., Schmid G., Ingino P., Li J., Neu T. R., Swanner E. D. and Kappler A. (2016) Binding of heavy metal ions in aggregates of microbial cells, EPS and biogenic iron minerals measured in-situ using metal-and glyco-conjugates-specific fluorophores. *Geochim. Cosmochim. Acta* **180**, 66–96.

Hardisty D. S., Lu Z., Planavsky N. J., Bekker A., Philippot P., Zhou X. and Lyons T. W. (2014) An iodine record of Paleoproterozoic surface ocean oxygenation. *Geology* **42**, 619–622.

Hartman H. (1984) The evolution of photosynthesis and microbial mats: a speculation on the banded iron formations. In *Microbial Mats: Stromatolites* (eds. Y. Cohen, R. W. Castenholz and H. O. Halvorson). Alan Liss, New York, pp. 451–453.

Hegler F., Posth N. R., Jiang J. and Kappler A. (2008) Physiology of phototrophic iron(II)-oxidizing bacteria: implications for modern and ancient environments. *FEMS Microbiol. Ecol.* **66**, 250–260.

Heimann A., Johnson C. M., Beard B. L., Valley J. W., Roden E. E., Spicuzza M. J. and Beukes N. J. (2010) Fe, C, and O isotope compositions of banded iron formation carbonates demonstrate a major role for dissimilatory iron reduction in ~2.5 Ga marine environments. *Earth Planet. Sci. Lett.* **294**, 8–18.

Heising S., Richter L., Ludwig W. and Schink B. (1999) *Chlorobium ferrooxidans* sp. nov., a phototrophic green sulfur bacterium that oxidizes ferrous iron in coculture with a "*Geospirillum*" sp. strain. *Arch. Microbiol.* **172**, 116–124.

Hempel G., Bischof K. and Hagen W. (2016) *Faszination Meeresforschung: Ein ökologisches Lesebuch*, second ed. Springer-Verlag, Berlin, Heidelberg.

Hiemstra T. (2018) Ferrihydrite interaction with silicate and competing oxyanions: geometry and hydrogen bonding of surface species. *Geochim. Cosmochim. Acta* **238**, 453–476.

Hinz I. L., Nims C., Theuer S., Templeton A. S. and Johnson J. E. (2021) Ferric iron triggers greenalite formation in simulated Archean seawater. *Geology* **49**, 905–910.

Hohmann C., Winkler E., Morin G. and Kappler A. (2009) Anaerobic Fe(II)-oxidizing bacteria show As resistance and immobilize As during Fe(III) mineral precipitation. *Environ. Sci. Technol.* **44**, 94–101.

Holland H. D. (1973) The oceans; a possible source of iron in iron-formations. *Econ. Geol.* **68**, 1169–1172.

Iler R. K. (1979) *Chemistry of Silica*. Wiley-Interscience, New York.

Imhoff J. F. (2014) The family *Chlorobiaceae*. In *The Prokaryotes* (eds. E. Rosenberg, E. F. DeLong, S. Lory, E. Stackebrandt and F. Thompson). Springer-Verlag, Berlin-Heidelberg.

Isley A. E. (1995) Hydrothermal plumes and the delivery of iron to banded iron formation. *J. Geol.* **103**, 169–185.

Jiang C. Z. and Tosca N. J. (2019) Fe(II)-carbonate precipitation kinetics and the chemistry of anoxic ferruginous seawater. *Earth Planet. Sci. Lett.* **506**, 231–242.

Jiang C. Z. and Tosca N. J. (2020) Growth kinetics of siderite at 298.15 K and 1 bar. *Geochim. Cosmochim. Acta* **274**, 97–117.

Jiao Y., Kappler A., Croal L. R. and Newman D. K. (2005) Isolation and characterization of a genetically tractable photoautotrophic Fe(II)-oxidizing bacterium, *Rhodopseudomonas palustris* strain TIE-1. *Appl. Environ. Microbiol.* **71**, 4487–4496.

Johnson C. M., Beard B. L., Beukes N. J., Klein C. and O'Leary J. M. (2003) Ancient geochemical cycling in the Earth as inferred from Fe isotope studies of banded iron formations from the Transvaal Craton. *Contrib. Mineral. Petrol.* **144**, 523–547.

Johnson C. M., Beard B. L., Klein C., Beukes N. J. and Roden E. E. (2008) Iron isotopes constrain biologic and abiologic processes in banded iron formation genesis. *Geochim. Cosmochim. Acta* **72**, 151–169.

Johnson C. M., Ludois J. M., Beard B. L., Beukes N. J. and Heimann A. (2013) Iron formation carbonates: paleoceanographic proxy or recorder of microbial diagenesis? *Geology* **41**, 1147–1150.

Johnson J. E., Muhling J. R., Cosmidis J., Rasmussen B. and Templeton A. S. (2018) Low-Fe (III) greenalite was a primary mineral from Neoarchean Oceans. *Geophys. Res. Lett.* **45**, 3182–3192.

Jones A. M., Collins R. N., Rose J. and Waite T. D. (2009) The effect of silica and natural organic matter on the Fe(II)-catalysed transformation and reactivity of Fe(III) minerals. *Geochim. Cosmochim. Acta* **73**, 4409–4422.

Jones C., Nomosatryo S., Crowe S. A., Bjerrum C. J. and Canfield D. E. (2015) Iron oxides, divalent cations, silica, and the early earth phosphorus crisis. *Geology* **43**, 135–138.

Kappler A. and Newman D. K. (2004) Formation of Fe(III)-minerals by Fe(II)-oxidizing photoautotrophic bacteria. *Geochim. Cosmochim. Acta* **68**, 1217–1226.

Kappler A., Bryce C., Mansor M., Lueder U., Byrne J. M. and Swanner E. D. (2021) An evolving view on biogeochemical cycling of iron. *Nat. Rev. Microbiol.* **19**, 360–374.

Kappler A., Pasquero C., Konhauser K. O. and Newman D. K. (2005) Deposition of banded iron formations by anoxygenic phototrophic Fe(II)-oxidizing bacteria. *Geology* **33**, 865–868.

Kaufman A. J., Hayes J. and Klein C. (1990) Primary and diagenetic controls of isotopic compositions of iron-formation carbonates. *Geochim. Cosmochim. Acta* **54**, 3461–3473.

Kendall B., Reinhard C. T., Lyons T. W., Kaufman A. J., Poulton S. W. and Anbar A. D. (2010) Pervasive oxygenation along late Archaean ocean margins. *Nat. Geosci.* **3**, 647–652.

Kingston F. J., Posner A. M. and Quirk J. P. (1972) Anion adsorption by goethite and gibbsite: I. The role of the proton in determining adsorption envelopes. *J. Soil Sci.* **23**, 177–192.

Klein C. (2005) Some Precambrian banded iron-formations (BIFs) from around the world: their age, geologic setting, mineralogy, metamorphism, geochemistry, and origins. *Am. Miner.* **90**, 1473–1499.

Klein C. and Beukes N. J. (1989) Geochemistry and sedimentology of a facies transition from limestone to iron-formation deposition in the early Proterozoic Transvaal Supergroup, South Africa. *Econ. Geol.* **84**, 1733–1774.

Klein C. and Beukes N. J. (1992) *Proterozoic iron-formations*. Elsevier, Netherlands, pp. 383–418.

Köhler I., Konhauser K. O., Papineau D., Bekker A. and Kappler A. (2013) Biological carbon precursor to diagenetic siderite with spherical structures in iron formations. *Nat. Commun.* **4**, 1–7.

Konhauser K. O., Newman D. K. and Kappler A. (2005) The potential significance of microbial Fe(III) reduction during

deposition of Precambrian banded iron formations. *Geobiology* **3**, 167–177.

Konhauser K. O., Planavsky N. J., Hardisty D. S., Robbins L. J., Warchola T. J., Haugaard R., Lalonde S. V., Partin C. A., Oonk P. B. H., Tsikos H., Lyons T. W., Bekker A. and Johnson C. M. (2017) Iron formations: a global record of Neoarchaean to Palaeoproterozoic environmental history. *Earth Sci. Rev.* **172**, 140–177.

Konhauser K. O., Hamade T., Raiswell R., Morris R. C., Ferris F. G., Southam G. and Canfield D. E. (2002) Could bacteria have formed the Precambrian banded iron formations? *Geology* **30**, 1079–1082.

Konhauser K. O., Lalonde S. V., Amskold L. and Holland H. D. (2007a) Was there really an Archean phosphate crisis? *Science* **315**, 1234–1234.

Konhauser K. O., Amskold L., Lalonde S. V., Posth N. R., Kappler A. and Anbar A. (2007b) Decoupling photochemical Fe(II) oxidation from shallow-water BIF deposition. *Earth Planet. Sci. Lett.* **258**, 87–100.

Krissansen-Totton J., Arney G. N. and Catling D. C. (2018) Constraining the climate and ocean pH of the early Earth with a geological carbon cycle model. *Proc. Natl. Acad. Sci.* **115**, 4105–4110.

Kukkadapu R. K., Zachara J. M., Fredrickson J. K. and Kennedy D. W. (2004) Biotransformation of two-line silica-ferrihydrite by a dissimilatory Fe(III)-reducing bacterium: formation of carbonate green rust in the presence of phosphate. *Geochim. Cosmochim. Acta* **68**, 2799–2814.

Kump L. R. and Seyfried W. E. (2005) Hydrothermal Fe fluxes during the Precambrian: effect of low oceanic sulfate concentrations and low hydrostatic pressure on the composition of black smokers. *Earth Planet. Sci. Lett.* **235**, 654–662.

Lalonde S. V., Konhauser K. O., Reysenbach A. L. and Ferris F. G. (2005) The experimental silicification of Aquificales and their role in hot spring sinter formation. *Geobiology* **3**, 41–52.

Laufer K., Niemeyer A., Nikeleit V., Halama M., Byrne J. M. and Kappler A. (2017) Physiological characterization of a halotolerant anoxygenic phototrophic Fe(II)-oxidizing green-sulfur bacterium isolated from a marine sediment. *FEMS Microbiol. Ecol.* **93**, fix054.

Laufer K., Nordhoff M., Røy H., Schmidt C., Behrens S., Jørgensen B. B. and Kappler A. (2016) Coexistence of microaerophilic, nitrate-reducing, and phototrophic Fe(II) oxidizers and Fe(III) reducers in coastal marine sediment. *Appl. Environ. Microbiol.* **82**, 1433–1447.

Li Y., Sutherland B. R., Gingras M. K., Owttrim G. W. and Konhauser K. O. (2021) A novel approach to investigate the deposition of (bio)chemical sediments: the sedimentation velocity of cyanobacteria–ferrihydrite aggregates. *J. Sediment. Res.* **91**, 390–398.

Li Y.-L., Konhauser K. O., Cole D. R. and Phelps T. J. (2011) Mineral ecophysiological data provide growing evidence for microbial activity in banded-iron formations. *Geology* **39**, 707–710.

Li Y.-L., Konhauser K. O., Kappler A. and Hao X.-L. (2013) Experimental low-grade alteration of biogenic magnetite indicates microbial involvement in generation of banded iron formations. *Earth Planet. Sci. Lett.* **361**, 229–237.

Li Y.-L., Konhauser K. O. and Zhai M. (2017) The formation of magnetite in the early Archean oceans. *Earth Planet. Sci. Lett.* **466**, 103–114.

Liljestrand F. L., Knoll A. H., Tosca N. J., Cohen P. A., Macdonald F. A., Peng Y. and Johnston D. T. (2020) The triple oxygen isotope composition of Precambrian chert. *Earth Planet. Sci. Lett.* **537** 116167.

Llirós M., García-Armisen T., Darchambeau F., Morana C., Triadó-Margarit X., Inceoğlu Ö., Borrego C. M., Bouillon S., Servais P. and Borges A. V. (2015) Pelagic photoferrotrophy and iron cycling in a modern ferruginous basin. *Sci. Rep.* **5**, 13803.

Lovley D. R. (1991) Magnetite formation during microbial dissimilatory iron reduction. In *Iron biominerals* (eds. R. B. Frankel and R. P. Blakemore). Springer, Boston, pp. 151–166.

Lovley D. R. and Phillips E. J. (1986) Organic matter mineralization with reduction of ferric iron in anaerobic sediments. *Appl. Environ. Microbiol.* **51**, 683–689.

Lovley D. R. and Phillips E. J. (1988) Novel mode of microbial energy metabolism: organic carbon oxidation coupled to dissimilatory reduction of iron or manganese. *Appl. Environ. Microbiol.* **54**, 1472–1480.

Lyons T. W., Reinhard C. T. and Planavsky N. J. (2014) The rise of oxygen in Earth's early ocean and atmosphere. *Nature* **506**, 307–315.

Maliva R. G., Knoll A. H. and Simonson B. M. (2005) Secular change in the Precambrian silica cycle: insights from chert petrology. *Geol. Soc. Am. Bull.* **117**, 835–845.

Manske A. K., Glaeser J., Kuypers M. M. and Overmann J. (2005) Physiology and phylogeny of green sulfur bacteria forming a monospecific phototrophic assemblage at a depth of 100 meters in the Black Sea. *Appl. Environ. Microbiol.* **71**, 8049–8060.

Martinez R. E., Konhauser K. O., Paunova N., Wu W., Alessi D. S. and Kappler A. (2016) Surface reactivity of the anaerobic phototrophic Fe(II)-oxidizing bacterium *Rhodovulum iodosum*: implications for trace metal budgets in ancient oceans and banded iron formations. *Chem. Geol.* **442**, 113–120.

Melton E. D., Schmidt C., Behrens S., Schink B. and Kappler A. (2014) Metabolic flexibility and substrate preference by the Fe (II)-oxidizing purple non-sulphur bacterium *Rhodopseudomonas palustris* strain TIE-1. *Geomicrobiol. J.* **31**, 835–843.

Mloszewska A. M., Cole D. B., Planavsky N. J., Kappler A., Whitford D. S., Owttrim G. W. and Konhauser K. O. (2018) UV radiation limited the expansion of cyanobacteria in early marine photic environments. *Nat. Commun.* **9**, 1–8.

Morris R. C. (1993) Genetic modelling for banded iron-formation of the Hamersley Group, Pilbara Craton, Western Australia. *Precambrian Res.* **60**, 243–286.

Muhling J. R. and Rasmussen B. (2020) Widespread deposition of greenalite to form Banded Iron Formations before the Great Oxidation Event. *Precambrian Res.* **339**, 105619.

Murad E. (1996) Magnetic properties of microcrystalline iron(III) oxides and related materials as reflected in their Mössbauer spectra. *Phys. Chem. Miner.* **23**, 248–262.

Murad E. (2010) Mossbauer spectroscopy of clays, soils and their mineral constituents. *Clay Miner.* **45**, 413–430.

Murad E., Bowen L., Long G. and Quin T. (1988) Influence of crystallinity on magnetic ordering in natural ferrihydrites. *Clay Miner.* **23**, 161–173.

Murad E. and Schwertmann U. (1980) The Möessbauer spectrum of ferrihydrite and its relations to those of other iron oxides. *Am. Mineral.* **65**, 1044–1049.

Nealson K. H. and Myers C. R. (1990) Iron reduction by bacteria: a potential role in the genesis of banded iron formations. *Am. J. Sci.* **290**, 35–45.

Olson S. L., Kump L. R. and Kasting J. F. (2013) Quantifying the areal extent and dissolved oxygen concentrations of Archean oxygen oases. *Chem. Geol.* **362**, 35–43.

O'Loughlin E. J., Gorski C. A., Flynn T. M. and Scherer M. M. (2019) Electron Donor Utilization and Secondary Mineral Formation during the Bioreduction of Lepidocrocite by *Shewanella putrefaciens* CN32. *Minerals* **9**, 434.

O'Loughlin E. J., Gorski C. A., Scherer M. M., Boyanov M. I. and Kemner K. M. (2010) Effects of oxyanions, natural organic matter, and bacterial cell numbers on the bioreduction of lepidocrocite (γ-FeOOH) and the formation of secondary mineralization products. *Environ. Sci. Technol.* **44**, 4570–4576.

Ostrander C. M., Nielsen S. G., Owens J. D., Kendall B., Gordon G. W., Romaniello S. J. and Anbar A. D. (2019) Fully oxygenated water columns over continental shelves before the Great Oxidation Event. *Nat. Geosci.* **12**, 186–191.

Ozaki K., Thompson K. J., Simister R. L., Crowe S. A. and Reinhard C. T. (2019) Anoxygenic photosynthesis and the delayed oxygenation of Earth's atmosphere. *Nat. Commun.* **10**, 1–10.

Pan W., Kan J., Inamdar S., Chen C. and Sparks D. (2016) Dissimilatory microbial iron reduction release DOC (dissolved organic carbon) from carbon-ferrihydrite association. *Soil Biol. Biochem.* **103**, 232–240.

Pantke C., Obst M., Benzerara K., Morin G., Ona-Nguema G., Dippon U. and Kappler A. (2012) Green Rust Formation during Fe(II) Oxidation by the Nitrate-Reducing *Acidovorax* sp. Strain BoFeN1. *Environ. Sci. Technol.* **46**, 1439–1446.

Pecoits E., Gingras M. K., Barley M. E., Kappler A., Posth N. R. and Konhauser K. O. (2009) Petrography and geochemistry of the Dales Gorge banded iron formation: paragenetic sequence, source and implications for palaeo-ocean chemistry. *Precambrian Res.* **172**, 163–187.

Peng C., Bryce C., Sundman A., Borch T. and Kappler A. (2019) Organic matter complexation promotes Fe(II) oxidation by the photoautotrophic Fe(II)-oxidizer *Rhodopseudomonas palustris* TIE-1. *ACS Earth Space Chem.* **3**, 531–536.

Percak-Dennett E. M., Beard B. L., Xu H., Konishi H., Johnson C. M. and Roden E. E. (2011) Iron isotope fractionation during microbial dissimilatory iron oxide reduction in simulated Archaean seawater. *Geobiology* **9**, 205–220.

Phoenix V. R., Konhauser K. O. and Ferris F. G. (2003) Experimental study of iron and silica immobilization by bacteria in mixed Fe-Si systems: implications for microbial silicification in hot springs. *Can. J. Earth Sci.* **40**, 1669–1678.

Poggenburg C., Mikutta R., Sander M., Schippers A., Marchanka A., Dohrmann R. and Guggenberger G. (2016) Microbial reduction of ferrihydrite-organic matter coprecipitates by *Shewanella putrefaciens* and *Geobacter metallireducens* in comparison to mediated electrochemical reduction. *Chem. Geol.* **447**, 133–147.

Poggenburg C., Mikutta R., Schippers A., Dohrmann R. and Guggenberger G. (2018) Impact of natural organic matter coatings on the microbial reduction of iron oxides. *Geochim. Cosmochim. Acta* **224**, 223–248.

Pokrovski G. S., Schott J., Farges F. and Hazemann J. L. (2003) Iron(III)-silica interactions in aqueous solution: insights from X-ray absorption fine structure spectroscopy. *Geochim. Cosmochim. Acta.* **67**, 3559–3573.

Pollak H. and Stevens J. G. (1986) Phyllosilicates: a Mössbauer evaluation. *Hyperfine Interact.* **29**, 1153–1156.

Posth N. R., Huelin S., Konhauser K. O. and Kappler A. (2010) Size, density and composition of cell-mineral aggregates formed during anoxygenic phototrophic Fe(II) oxidation: impact on modern and ancient environments. *Geochim. Cosmochim. Acta* **74**, 3476–3493.

Posth N. R., Köhler I., Swanner E. D., Schröder C., Wellmann E., Binder B., Konhauser K. O., Neumann U., Berthold C., Nowak M. and Kappler A. (2013) Simulating Precambrian banded iron formation diagenesis. *Chem. Geol.* **362**, 66–73.

Postma D. (1993) The reactivity of iron oxides in sediments: a kinetic approach. *Geochim. Cosmochim. Acta* **57**, 5027–5034.

Poulton S. W., Bekker A., Cumming V. M., Zerkle A. L., Canfield D. E. and Johnston D. T. (2021) A 200-million-year delay in permanent atmospheric oxygenation. *Nature* **592**, 232–236.

Rasmussen B. and Muhling J. R. (2018) Making magnetite late again: evidence for widespread magnetite growth by thermal decomposition of siderite in Hamersley banded iron formations. *Precambrian Res.* **306**, 64–93.

Rasmussen B., Meier D. B., Krapež B. and Muhling J. R. (2013) Iron silicate microgranules as precursor sediments to 2.5-billion-year-old banded iron formations. *Geology* **41**, 435–438.

Rasmussen B., Krapež B., Muhling J. R. and Suvorova A. (2015) Precipitation of iron silicate nanoparticles in early Precambrian oceans marks Earth's first iron age. *Geology* **43**, 303–306.

Rasmussen B., Muhling J. R., Suvorova A. and Krapež B. (2017) Greenalite precipitation linked to the deposition of banded iron formations downslope from a late Archean carbonate platform. *Precambrian Res.* **290**, 49–62.

Rasmussen B., Muhling J. R. and Fischer W. W. (2020) Greenalite Nanoparticles in Alkaline Vent Plumes as Templates for the Origin of Life. *Astrobiology* **21**, 246–259.

Rasmussen B., Muhling J. R. and Krapež B. (2021) Greenalite and its role in the genesis of early Precambrian iron formations – A review. *Earth-Sci. Rev.* **103613**.

Reddy T. R., Zheng X.-Y., Roden E. E., Beard B. L. and Johnson C. M. (2016) Silicon isotope fractionation during microbial reduction of Fe(III)–Si gels under Archean seawater conditions and implications for iron formation genesis. *Geochimica et Cosmochimica Acta* **190**, 85–99.

Repeta D. J., Simpson D. J., Jorgensen B. B. and Jannasch H. W. (1989) Evidence for anoxygenic photosynthesis from the distribution of bacterio-chlorophylls in the Black Sea. *Nature* **342**, 69–72.

Robbins L. J., Funk S. P., Flynn S. L., Warchola T. J., Li Z., Lalonde S. V., Rostron B. J., Smith A. J. B., Beukes N. J., de Kock M. O., Heaman L. M., Alessi D. S. and Konhauser K. O. (2019) Hydrogeological constraints on the formation of Palaeoproterozoic banded iron formations. *Nat. Geosci.* **12**, 558–563.

Roden E. E. (2003) Fe(III) oxide reactivity toward biological versus chemical reduction. *Environ. Sci. Technol.* **37**, 1319–1324.

Roden E. E. and Zachara J. M. (1996) Microbial reduction of crystalline iron(III) oxides: influence of oxide surface area and potential for cell growth. *Environ. Sci. Technol.* **30**, 1618–1628.

Roland F. A. E., Borges A. V., Darchambeau F., Llirós M., Descy J. P. and Morana C. (2021) The possible occurrence of iron-dependent anaerobic methane oxidation in an Archean Ocean analogue. *Sci. Rep.* **11**, 1–11.

Schad M., Halama M., Bishop B., Konhauser K. O. and Kappler A. (2019) Temperature fluctuations in the Archean ocean as trigger for varve-like deposition of iron and silica minerals in banded iron formations. *Geochim. Cosmochim. Acta* **265**, 386–412.

Schwertmann U. and Cornell R. M. (2008) *Iron oxides in the laboratory*. John Wiley & Sons.

Schwertmann U. and Fechter H. (1982) The point of zero charge of natural and synthetic ferrihydrites and its relation to adsorbed silicate. *Clay Miner.* **17**, 471–476.

Schwertmann U., Friedl J. and Kyek A. (2004) Formation and properties of a continuous crystallinity series of synthetic ferrihydrites (2-to 6-line) and their relation to FeOOH forms. *Clays Clay Miner.* **52**, 221–226.

Sengupta S., Peters S. T., Reitner J., Duda J. P. and Pack A. (2020) Triple oxygen isotopes of cherts through time. *Chem. Geol.* **554**, 119789.

Shimizu M., Zhou J., Schröder C., Obst M., Kappler A. and Borch T. (2013) Dissimilatory reduction and transformation of

ferrihydrite-humic acid coprecipitates. *Environ. Sci Technol.* **47**, 13375–13384.

Siahi M., Tsikos H., Rafuza S., Oonk P. B., Mhlanga X. R., van Niekerk D., Mason P. R. D. and Harris C. (2020) Insights into the processes and controls on the absolute abundance and distribution of manganese in Precambrian iron formations. *Precamb. Res.* **350**, 105878.

Siever R. (1992) The silica cycle in the Precambrian. *Geochim. Cosmochim. Acta* **56**, 3265–3272.

Sigg L. and Stumm W. (1981) The interaction of anions and weak acids with the hydrous goethite (α-FeOOH) surface. *Colloid. Surface.* **2**, 101–117.

Simon L., François M., Refait P., Renaudin G., Lelaurain M. and Génin J. M. R. (2003) Structure of the Fe(II-III) layered double hydroxysulphate green rust two from Rietveld analysis. *Solid State Sci.* **5**, 327–334.

Steinhoefel G., von Blanckenburg F., Horn I., Konhauser K. O., Beukes N. J. and Gutzmer J. (2010) Deciphering formation processes of banded iron formations from the Transvaal and the Hamersley successions by combined Si and Fe isotope analysis using UV femtosecond laser ablation. *Geochim. Cosmochim. Acta* **74**, 2677–2696.

Stewart R. H. (2008) *Introduction to physical oceanography*. Robert H. Stewart.

Stookey L. L. (1970) Ferrozine - a new spectrophotometric reagent for iron. *Anal. Chem.* **42**, 779–781.

Straub K. L., Rainey F. A. and Widdel F. (1999) *Rhodovulum iodosum* sp. nov. and *Rhodovulum robiginosum* sp. nov., two new marine phototrophic ferrous-iron-oxidizing purple bacteria. *Int. J. Syst. Bacteriol.* **49**, 729–735.

Strickland J. D. H. and Parsons T. R. (1972). In *A practical handbook of seawater analysis*. Fisheries Research Board of Canada, Ottawa, p. 167.

Swanner E. D., Mloszewska A. M., Cirpka O. A., Schoenberg R., Konhauser K. O. and Kappler A. (2015) Modulation of oxygen production in Archaean oceans by episodes of Fe(II) toxicity. *Nat. Geosci.* **8**, 126–130.

Swedlund P. J. and Webster J. G. (1999) Adsorption and polymerisation of silicic acid on ferrihydrite, and its effect on arsenic adsorption. *Water Res.* **33**, 3413–3422.

Swedlund P. J., Miskelly G. M. and McQuillan A. J. (2010) Silicic acid adsorption and oligomerization at the ferrihydrite-water interface: interpretation of ATR-IR spectra based on a model surface structure. *Langmuir* **26**, 3394–3401.

Teixeira N. L., Caxito F. A., Rosière C. A., Pecoits E., Vieira L., Frei R., Sial A. N. and Poitrasson F. (2017) Trace elements and isotope geochemistry (C, O, Fe, Cr) of the Cauê iron formation, Quadrilátero Ferrífero, Brazil: evidence for widespread microbial dissimilatory iron reduction at the Archean/Paleoproterozoic transition. *Precambrian Res.* **298**, 39–55.

Thibon F., Blichert-Toft J., Tsikos H., Foden J., Albalat E. and Albarede F. (2019) Dynamics of oceanic iron prior to the Great Oxygenation Event. *Earth Planet. Sci. Lett.* **506**, 360–370.

ThomasArrigo L. K., Mikutta C., Byrne J. M., Kappler A. and Kretzschmar R. (2017) Iron(II)-catalyzed iron atom exchange and mineralogical changes in iron-rich organic freshwater flocs: an iron isotope tracer study. *Environ. Sci. Technol.* **51**, 6897–6907.

Thompson K. J., Kenward P. A., Bauer K. W., Warchola T., Gauger T., Martinez R., Simister R. L., Michiels C. C., Llirós M., Reinhard C. T., Kappler A., Konhauser K. O. and Crowe S. A. (2019) Photoferrotrophy, deposition of banded iron formations, and methane production in Archean oceans. *Sci. Adv.* **5**, eaav2869.

Tosca N. J., Guggenheim S. and Pufahl P. K. (2016) An authigenic origin for Precambrian greenalite: implications for iron formation and the chemistry of ancient seawater. *Geol. Soc. Am. Bull.* **128**, 511–530.

Trendall A. F. (2002) The significance of iron-formation in the Precambrian stratigraphic record. Precambrian Sedimentary Environments: a Modern Approach to Depositional Systems. *Spec. Publ. Internat. Assoc. Sedimentol.* **33**, 33–66.

Trendall A. F. and Blockley J. B. (1970) The iron formations of the Hamersley Group, Western Australia, with special reference to the associated crocidolite. *Western Austr. Geol. Surv., Bull.* **119**, 353 pp.

Walker J. C. (1984) Suboxic diagenesis in banded iron formations. *Nature* **309**, 340–342.

Wang C., Konhauser K. O. and Zhang L. (2015) Depositional environment of the Paleoproterozoic Yuanjiacun banded iron formation in Shanxi Province, China. *Econ. Geol.* **110**, 1515–1539.

Wang X., Kubicki J. D., Boily J.-F., Waychunas G. A., Hu Y., Feng X. and Zhu M. (2018) Binding geometries of silicate species on ferrihydrite surfaces. *ACS Earth Space Chem.* **2**, 125–134.

Wu L., Percak-Dennett E. M., Beard B. L., Roden E. E. and Johnson C. M. (2012) Stable iron isotope fractionation between aqueous Fe(II) and model Archean ocean Fe–Si coprecipitates and implications for iron isotope variations in the ancient rock record. *Geochim. Cosmochim. Acta* **84**, 14–28.

Wu W., Swanner E. D., Hao L., Zeitvogel F., Obst M., Pan Y. and Kappler A. (2014) Characterization of the physiology and cell-mineral interactions of the marine anoxygenic phototrophic Fe (II) oxidizer *Rhodovulum iodosum* – implications for Precambrian Fe(II) oxidation. *FEMS Microbiol. Ecol.* **88**, 503–515.

Wu W., Swanner E. D., Kleinhanns I. C., Schoenberg R., Pan Y. and Kappler A. (2017) Fe isotope fractionation during Fe(II) oxidation by the marine photoferrotroph *Rhodovulum iodosum* in the presence of Si - implications for Precambrian iron formation deposition. *Geochim. Cosmochim. Acta* **211**, 307–321.

Zachara J. M., Kukkadapu R. K., Fredrickson J. K., Gorby Y. A. and Smith S. C. (2002) Biomineralization of poorly crystalline Fe(III) oxides by dissimilatory metal reducing bacteria (DMRB). *Geomicrobiol. J.* **19**, 179–207.

Zagorac D., Müller H., Ruehl S., Zagorac J. and Rehme S. (2019) Recent developments in the Inorganic Crystal Structure Database: theoretical crystal structure data and related features. *J. Appl. Crystallogr.* **52**, 918–925.

Zakharov D. O., Marin-Carbonne J., Alleon J. and Bindeman I. N. (2021) Triple oxygen isotope trend recorded by Precambrian cherts: a perspective from combined bulk and in situ secondary ion probe measurements. *Rev. Mineral. Geochem.* **86**, 323–365.

Zegeye A., Bonneville S., Benning L. G., Sturm A., Fowle D. A., Jones C., Canfield D. E., Ruby C., MacLean L. C., Nomosatryo S., Crowe S. A. and Poulton S. W. (2012) Green rust formation controls nutrient availability in a ferruginous water column. *Geology* **40**, 599–602.

Zeng Z. and Tice M. M. (2014) Promotion and nucleation of carbonate precipitation during microbial iron reduction. *Geobiology* **12**, 362–371.

Zheng X.-Y., Beard B. L., Reddy T. R., Roden E. E. and Johnson C. M. (2016) Abiologic silicon isotope fractionation between aqueous Si and Fe(III)–Si gel in simulated Archean seawater: implications for Si isotope records in Precambrian sedimentary rocks. *Geochim. Cosmochim. Acta* **187**, 102–122.

Zhou Z., Latta D. E., Noor N., Thompson A., Borch T. and Scherer M. M. (2018) Fe(II)-catalyzed transformation of organic matter-ferrihydrite coprecipitates: a closer look using Fe isotopes. *Environ. Sci. Technol.* **52**, 11142–11150.

Associate editor: Brandy Marie Toner